J. Fluid Mech. (2019), *vol.* 858, *pp.* 228–263.
doi:10.1017/jfm.2018.782

Jet formation in salt-finger convection: a modified Rayleigh–Bénard problem

Jin-Han Xie[1,†], Keith Julien[2] and Edgar Knobloch[3]

[1]Courant Institute of Mathematical Sciences, New York University, New York, NY 10012, USA

[2]Department of Applied Mathematics, University of Colorado, Boulder, CO 80309, USA

[3]Department of Physics, University of California, Berkeley, CA 94720, USA

(Received 8 March 2018; revised 26 September 2018; accepted 27 September 2018; first published online 2 November 2018)

Large-scale coherent structures such as jets in Rayleigh–Bénard convection and related systems are receiving increasing attention. This paper studies, both numerically and theoretically, the process of jet formation in two-dimensional salt-finger convection. The approach utilizes an asymptotically derived system of equations referred to as the modified Rayleigh–Bénard convection (MRBC) model, valid in the geophysically and astrophysically relevant limit in which the solute diffuses much more slowly than heat. In these equations, convection is driven by a destabilizing salinity gradient while the effects of the stabilizing temperature gradient manifest themselves as an additional anisotropic dissipation acting on large scales. The MRBC system is specified by two external parameters: the Schmidt number Sc (ratio of viscosity to solutal diffusivity) and the Rayleigh ratio Ra (ratio between the Rayleigh numbers of the destabilizing solutal stratification and the stabilizing thermal stratification). Two distinct Ra regimes are explored for fixed $Sc = 1$. In all cases studied the system develops a horizontal jet structure that is maintained self-consistently by turbulent fluctuations, but coarsens over time. For intermediate Rayleigh ratios (e.g. $Ra = 6$), the MRBC model captures the relaxation oscillations superposed on the jet structure observed at similar parameter values in direct numerical simulations of the primitive equations. For smaller Rayleigh ratios (e.g. $Ra = 2$), a regime for which direct numerical simulation of the primitive equations is difficult because of the presence of fast gravity waves, the MRBC model reveals the existence of statistically steady jets whose properties are studied in detail. Three hierarchical models, the MRBC and further reductions in the form of quasilinear and single-mode approximations, are used to confirm that jets form and are sustained as a result of the interaction between fluctuations (salt fingers) and large-scale horizontally averaged horizontal flows (jets). Even though the small-scale structures exhibited by the three models exhibit clear differences, all three produce the same power-law spectrum of the mean fields at large vertical scales: in all, the spectrum of the mean streamfunction scales as m^{-3} and the mean salinity field scales as m^{-1}, with m the vertical wavenumber. A theoretical explanation of these observations based on the dominant balances in the mean and fluctuation equations is provided. As a consequence, the jets have a zigzag profile, a conclusion that is consistent with numerical simulations. Based on numerical observations, a three-component phenomenological model consisting of a linearly growing mode, a linearly damped mode and a mean mode is proposed

† Email address for correspondence: jhxie@cims.nyu.edu

to explain the observed transition from statistically steady jet structure to jets with superposed oscillations that takes place with increasing Rayleigh ratio.

Key words: convection, double diffusive convection, jets

1. Introduction

Salt-finger convection (SFC) occurs in stably stratified fluids where warm salty water overlies cool fresh water and is driven by differential diffusivities of salt and heat. The instability requires that the ratio τ of the solutal to thermal diffusivity (or inverse Lewis number) satisfies $\tau < 1$, i.e. that heat diffuses more rapidly than salt (Turner 1974; Schmitt 1994; Merryfield, Holloway & Gargett 1999; Radko 2013). Similar processes arise in other geophysical and astrophysical situations involving competing fields whenever the destabilizing field diffuses more slowly than the stabilizing field (Schmitt 1983).

Stern (1960) was the first to study the onset of the salt-finger instability. However, as the amplitude of the linearly unstable salt-finger mode grows, secondary instabilities are triggered (Holyer 1984), initializing processes that ultimately lead to a statistically saturated state that may consist of large-scale structures embedded in a field of fluctuations. Stern (1969) developed from first principles the notion of collective instability, a particular case of secondary instability, to explain the saturation of the salt-finger instability, and proposed a dimensionless number now known as the Stern number as the key parameter in the saturation process. Further progress was made by Radko & Smith (2012), who proposed that saturation begins when the growth rate of the secondary finger instability becomes comparable to that of the primary salt-finger instability. Finger collisions may also contribute to saturation (Shen 1995). The saturation process itself is complicated by the presence of scales larger than the finger scale (Radko 2008). These may take the form of salt-rich blobs or modons (Radko 2008) or finger-generated large-scale flows (Garaud & Brummell 2015). Recently, Xie *et al.* (2017) formulated a two-dimensional reduced model to address some of these questions in a more tractable setting. This model is derived in the limit of small diffusivity ratio, $\tau \ll 1$, large thermal to solutal density ratio, $R_\rho \gg 1$, and infinite Schmidt number Sc, a situation relevant to the oceans. Here Sc is the ratio between viscosity and solutal diffusivity. Xie *et al.* (2017) find that the generation of large-scale structures depends strongly on the Rayleigh ratio Ra, the ratio between the saline and thermal Rayleigh numbers, and conclude that large-scale structures are crucial to the saturation process when the Rayleigh ratio is large, but unimportant otherwise.

Among the large-scale structures arising in salt-finger convection, the most striking example is provided by the thermohaline staircase (Radko 2013). Staircase formation is intimately related to the dominant saturation mechanism of the salt-finger instability. Stern's (1969) theory explains the onset of incipient staircases, but does not describe the dynamics leading to the establishment of fully developed staircases. Paparella & von Hardenberg (2012) discuss the formation of thermohaline staircases using a density flux theory for stably stratified fluids, originally proposed by Balmforth, Llewellyn Smith & Young (1998). A largely successful but phenomenological flux-based theory, the γ-instability theory, was proposed by Radko (2003) and generalized by Traxler *et al.* (2011*b*) and Stellmach *et al.* (2011). The resulting

theory is consistent with existing direct numerical simulations and was applied to astrophysical fingering convection by Brown, Garaud & Stellmach (2013).

In addition to staircase formation, large-scale horizontal velocities or jets represent another type of geophysically important layered structure. In two-dimensional salt-finger convection, jets were first observed by Radko (2010) in reduced models for weakly nonlinear salt fingers and later by Garaud & Brummell (2015) in direct numerical simulations of the primitive equations. In addition, jets have also been studied using low-order truncated models (Paparella & Spiegel 1999). This paper aims at understanding the basic mechanisms behind jet formation in salt-finger convection by focusing on an asymptotic model also valid in the limit $\tau \to 0$, but this time with $Sc = O(1)$ (Xie *et al.* 2017). This regime thus corresponds to low Prandtl numbers, and so is pertinent to astrophysical objects (Traxler, Garaud & Stellmach 2011*a*; Brown *et al.* 2013; Prat, Lignières & Lagarde 2015; Garaud 2018). In contrast, the regime $Sc \gg 1$, $Pr = O(1)$ studied by Xie *et al.* (2017) is relevant to terrestrial oceans.

In the following we refer to this model as the modified Rayleigh–Bénard convection (MRBC) model since the governing equations resemble those for Rayleigh–Bénard convection (RBC) except for the presence of large-scale anisotropic damping arising from thermal effects that are otherwise eliminated in the asymptotic procedure. The model thus represents a connection between SFC and RBC, and as such merits study in its own right (Chong *et al.* 2017). We mention that large-scale shear flows in RBC were originally observed by Malkus (1954) and Krishnamurti & Howard (1981), and studied extensively within both low-order truncated models (Howard & Krishnamurti 1986; Hermiz, Guzdar & Finn 1995; Childress 2000) and direct numerical simulations in two dimensions (Fitzgerald & Farrell 2014; Goluskin *et al.* 2014). Other RBC-related systems with jet formation include rotating convection (Busse 1983; Brummell & Hart 1993; von Hardenberg *et al.* 2015), plasma flows in tokamaks (Horton, Hu & Laval 1996) and magnetoconvection (Matthews *et al.* 1993; Rucklidge & Matthews 1996).

Although direct numerical simulations (DNS) of the primitive equations provide invaluable information and can be used to identify essential mechanisms (e.g. Traxler *et al.* 2011*b*), reduced models derived by a systematic mathematical procedure are expected to preserve key features of the primitive equations within a simpler formulation. They can therefore be used to probe extreme parameter regimes that are inaccessible to the DNS approach (Stern & Radko 1998; Radko & Stern 1999; Prat *et al.* 2015). For example, in the investigations carried out by Garaud & Brummell (2015), the buoyancy frequency of a stably stratified layer places strong limitations on the achievable temporal resolution. As a result, the accessible density ratios are significantly below $R_\rho \tau = O(1)$ when $\tau \ll 1$, a parameter regime of interest for stars on the red giant branch (Denissenkov 2010). In contrast, the MRBC model studied here is derived specifically for the case $R_\rho \tau = O(1)$ and $\tau \ll 1$, and enables a detailed exploration of this extreme regime at much lower cost than typical DNS studies performed well below $R_\rho \tau = O(1)$.

In this paper we use the asymptotically derived MRBC model to study two-dimensional SFC in doubly periodic domains instead of vertically bounded domains. This formulation avoids complications that arise from the formation of boundary layers and associated effects, and is justified *a posteriori* by the presence of an intrinsic length scale in the problem – a length scale independent of the domain size. The MRBC model inherits this property of SFC through the presence of large-scale damping, which makes the doubly periodic domain set-up appropriate for a study

of domain-size-independent properties. Because of this property the MRBC model represents a natural generalization of the two-dimensional vorticity equation with large-scale Rayleigh friction, driven by prescribed small-scale random forcing (Smith & Yakhot 1994; Bouchet & Simonnet 2009; Laurie *et al.* 2014; Frishman 2017; Frishman, Laurie & Falkovich 2017). However, in contrast to the vorticity problem, in our system the large-scale structures that form interact with and modify the fluctuations that sustain them.

The structure of the paper is as follows. In § 2 we formulate the reduced MRBC model and summarize its linear stability properties. In § 3 we report on two representative sets of numerical simulations, with $Ra = 6$ (§ 3.1) and with $Ra = 2$ (§ 3.2), both for $Sc = 1$. The former captures the relaxation oscillations observed in simulations of the primitive equations at intermediate density ratios by Garaud & Brummell (2015), thereby validating the MRBC model. In the latter regime, our simulations approach the regime of very large density ratios, $R_\rho \sim \tau^{-1} \gg 1$, that is at present inaccessible to DNS of the primitive equations owing to the presence of fast gravity waves, and show that this regime is characterized by quasi-steady jet-like structures that coarsen over time. We show that the jets are the result of an interaction between the fluctuations and the mean, and perform in § 4 two further reductions of the MRBC system based on this understanding. We show that these reductions preserve the essential physics of the jet formation problem, and utilize our findings in § 5 to extract universal spectral scalings for the large-scale mean fields. Finally, in § 6 we use the simulation results to motivate a phenomenological model that captures the transition from statistically steady jets at $Ra = 2$ to the oscillating jets present at larger Ra. Our results are summarized along with concluding remarks in § 7.

2. Formulation and linear stability

The two-dimensional modified Rayleigh–Bénard convection (MRBC) model filters out fast gravity waves and hence represents a projection of the primitive equations onto the slow manifold. As a result, the model is suitable for studying strongly driven systems in which gravity wave frequencies are high and the simulation of the primitive equations prohibitively expensive. In two dimensions the dimensionless model equations take the form (Xie *et al.* 2017)

$$\frac{1}{Sc}\left[\frac{\partial}{\partial t}\nabla^2\psi + \mathcal{J}(\psi, \nabla^2\psi)\right] = -\frac{\partial S}{\partial x} + (\Delta^{-1}\partial_{xx} + \nabla^4)\psi, \tag{2.1a}$$

$$\frac{\partial}{\partial t}S + \mathcal{J}(\psi, S) + Ra\frac{\partial \psi}{\partial x} = \nabla^2 S. \tag{2.1b}$$

Here ψ is the streamfunction while S denotes the perturbation salinity field around a destabilizing linear salinity gradient, with $\mathcal{J}(a, b) \equiv a_x b_z - a_z b_x$ and Δ^{-1} the inverse Laplacian operator. Owing to rapid thermal diffusion, the temperature field is slaved to the velocity field and is therefore no longer present; its effect manifests itself in the presence of a new dissipative term in (2.1*a*) corresponding to large-scale thermal damping. The novel feature of the MRBC model is thus the simultaneous presence of both small-scale (viscous) and large-scale (thermal) dissipation. As a result (2.1) defines a characteristic instability scale that is unrelated to the layer height. This new property alone makes the MRBC model worthy of detailed study.

The dimensionless quantities present in (2.1) are defined as follows:

$$t = \frac{\kappa_S}{d^2}t^*, \quad (x,\ z) = \frac{1}{d}(x^*,\ z^*), \quad \psi = \frac{1}{\kappa_S}\psi^* \quad \text{and} \quad S = \frac{R_\rho \tau}{\beta_S d}S^*, \tag{2.2a–d}$$

where * indicates dimensional quantities and

$$d = \left(\frac{\nu \kappa_T}{g \alpha_T \beta_T} \right)^{1/4} \tag{2.3}$$

is the (dimensional) natural finger scale.

The MRBC model describes salt-finger convection in the limit $\tau \to 0$, $R_\rho \to \infty$, a regime described by two independent dimensionless parameters instead of the usual three, the Prandtl number $Pr \equiv \nu/\kappa_T$, the density ratio $R_\rho \equiv \alpha_T \beta_T/(\alpha_S \beta_S)$ and the diffusivity ratio $\tau \equiv \kappa_S/\kappa_T$. The model assumes that these two remaining parameters, the Rayleigh ratio

$$Ra \equiv \frac{1}{R_\rho \tau} = \frac{Ra_S}{Ra_T} \tag{2.4}$$

and the Schmidt number $Sc \equiv \nu/\kappa_S$, both remain of order one. Here

$$Ra_T = \frac{g \alpha_T \beta_T H^4}{\nu \kappa_T} \quad \text{and} \quad Ra_S = \frac{g \alpha_S \beta_S H^4}{\nu \kappa_S} \tag{2.5a,b}$$

are the usual thermal and solutal Rayleigh numbers characterizing the stabilizing temperature and destabilizing salinity profiles. In these expressions $\alpha_{T,S}$ are the expansion coefficients, $\kappa_{T,S}$ are the diffusivities, $\beta_{T,S}$ are the background gradients, g is the gravitational acceleration, H is the layer depth and ν is the kinematic viscosity; the subscripts T and S denote temperature and salinity, respectively. When τ is small, i.e. when the temperature field diffuses much more rapidly than salinity, the above regime corresponds to strong driving via an unstable salt stratification. In this regime the temperature field is slaved to the velocity field and may be eliminated from the governing equations via a systematic asymptotic expansion in the small parameter τ (Xie *et al.* 2017). Equations (2.1) represent the leading-order description of the system to within $O(\tau)$ corrections.

To relate the intrinsic scale for salt-finger convection to the scale d we substitute a normal mode ansatz of the form $(\psi, S) = \mathrm{e}^{\lambda t + \mathrm{i}(kx+mz)}(\psi_0, S_0)$ into (2.1), linearized around $S = \psi = 0$. We find that the linear growth rate λ satisfies

$$\lambda^2 + \left[|\boldsymbol{k}|^2 + \frac{Sc}{|\boldsymbol{k}|^4}(k^2 + |\boldsymbol{k}|^6) \right] \lambda + \frac{Sc}{|\boldsymbol{k}|^2}(k^2 + |\boldsymbol{k}|^6 - Rak^2) = 0, \tag{2.6}$$

where $|\boldsymbol{k}|^2 = k^2 + m^2$. This equation informs us that linear instability is present only when the last term is negative, i.e. when

$$Ra > Ra(k, m) \equiv 1 + \frac{|\boldsymbol{k}|^6}{k^2}. \tag{2.7}$$

This condition is independent of Sc and so applies even in the limit $Sc \to \infty$ appropriate for terrestrial oceans. The critical value of Ra for linear instability is thus $Ra_c = 1$ and the instability sets in with wavenumbers $(k, m) = (0, 0)$. In the following we find that the quantity $\mathcal{R} \equiv Ra - 1$ provides a convenient measure of the distance from threshold, i.e. the supercriticality of the system. The positive (unstable) solution

of (2.6) is

$$\lambda = \frac{1}{2}\left(-\left[|\boldsymbol{k}|^2 + \frac{Sc}{|\boldsymbol{k}|^4}(k^2 + |\boldsymbol{k}|^6)\right] + \sqrt{\left[|\boldsymbol{k}|^2 + \frac{Sc}{|\boldsymbol{k}|^4}(k^2 + |\boldsymbol{k}|^6)\right]^2 - \frac{4Sc}{|\boldsymbol{k}|^2}(k^2 + |\boldsymbol{k}|^6 - Rak^2)}\right), \tag{2.8}$$

which reduces in the limit of $Sc \to \infty$ to the growth rate of the inertia-free salt-finger convection (IFSC) model derived by Xie *et al.* (2017):

$$\lambda_{IFSC} = Ra\frac{k^2|\boldsymbol{k}|^2}{k^2 + |\boldsymbol{k}|^6} - |\boldsymbol{k}|^2. \tag{2.9}$$

When the supercriticality $\mathcal{R}$ is small, we find that the optimal growth rate behaves like

$$\lambda_{opt} = \frac{2}{3^{3/2}}\mathcal{R}^{3/2} + \text{h.o.t.}, \tag{2.10}$$

a quantity independent of Sc to leading order, and hence identical to that for $Sc = \infty$ (Xie *et al.* 2017, equation (26b)), matching the small-Pr result of Brown *et al.* (2013, equation (B20)).

The linear growth rate $\lambda(k, m)$ for $Ra = 2$ and $Ra = 6$ and three different values of Sc is shown in figure 1. The figure highlights the anisotropic dependence of λ on k and m: for fixed m, not too large, there exists an optimal k that maximizes the growth rate, whereas when k is fixed, an optimal m exists for small k, but for large k the growth rate decreases monotonically with increasing m. The sequence of plots in each column shows that the linear growth rate and the horizontal wavenumber k of the most unstable mode increase with increasing Sc, and we find that they reach a regular limit as $Sc \to \infty$. The most unstable modes are the so-called elevator modes with $m = 0$. These modes are unstable within a band of horizontal wavenumbers k that is well captured by the supercriticality $\mathcal{R}$,

$$0 < k^4 < \mathcal{R}, \tag{2.11}$$

and are exact solutions of the nonlinear equations (2.1) with periodic boundary conditions in the vertical. However, in contrast to the IFSC model valid in the limit $Sc \to \infty$, these modes are not directly involved in the saturation process. The reasons for this difference are elaborated below.

3. Nonlinear simulations

In this section, we present two representative numerical simulations of the MRBC system (2.1). These use a Fourier pseudospectral method with 2/3 dealiasing in space with resolution 512×512 and a fourth-order explicit Runge–Kutta scheme in time with a fixed time step 5×10^{-3} in which the nonlinear terms are treated explicitly and linear terms implicitly using an integrating factor method. All calculations are initialized with small-amplitude random Gaussian fields whose amplitude determines the time required to reach saturation. The numerical results provide an empirical foundation for the theoretical development in later sections.

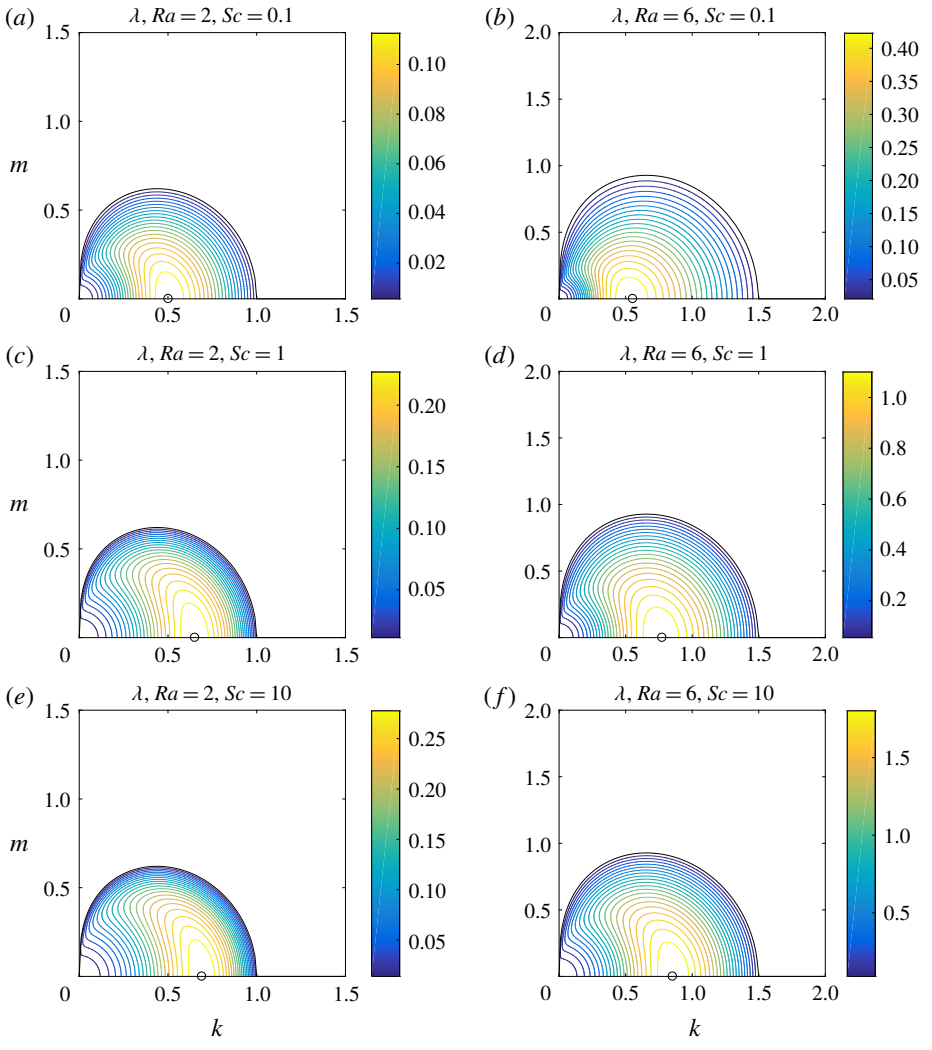

FIGURE 1. (Colour online) Contour plots of the linear growth rate $\lambda(k, m)$ of the MRBC model (2.1) defined in (2.8). Results for $Ra = 2$ (*a*,*c*,*e*) and $Ra = 6$ (*b*,*d*,*f*), respectively, for $Sc = 0.1$ (*a*,*b*), 1 (*c*,*d*) and 10 (*e*,*f*). Only positive growth rates are shown. Circles mark the optimal wavenumbers: 0.50, 0.65 and 0.68 for $Ra = 2$ and increasing Sc, approaching the optimal wavenumber 0.69 when $Sc = \infty$; and 0.55, 0.77 and 0.85 for $Ra = 6$ and increasing Sc, approaching the optimal wavenumber 0.88 when $Sc = \infty$.

3.1. *Simulation of the MRBC system with* $Ra = 6$, $Sc = 1$

We begin with the case $Ra = 6$, $Sc = 1$. This case corresponds to high-density-ratio simulations of two-dimensional salt-finger convection using primitive equations by Garaud & Brummell (2015), and therefore permits validation of the MRBC system. We present here the results of a simulation initialized with small homogeneous random perturbations ψ and S in a doubly periodic domain of size $L_x \times L_z \equiv 32 l_{opt} \times 32 l_{opt}$. Here $l_{opt} = 2\pi/k_{opt}$ is the wavelength of the fastest growing mode in the limit $Sc \to \infty$,

where

$$k_{opt}^4 = \tfrac{1}{2}(-2 - Ra + \sqrt{Ra^2 + 8Ra}). \tag{3.1}$$

In figure 2 we show the time evolution of the salinity potential energy P_S, the salinity flux F_S, the kinetic energy K_{jet} in the jets that form and the fluctuation kinetic energy K_{fluc}, defined as follows:

$$P_S = \frac{1}{2A}\int S^2 \,\mathrm{d}x\,\mathrm{d}z, \tag{3.2a}$$

$$F_S = \frac{1}{A}\int \psi_x S \,\mathrm{d}x\,\mathrm{d}z, \tag{3.2b}$$

$$K_{tot} = \frac{1}{2A}\int \left[(\psi_x)^2 + (\psi_z)^2\right] \,\mathrm{d}x\,\mathrm{d}z, \tag{3.2c}$$

$$K_{jet} = \frac{1}{2L_z}\int \left(\frac{1}{L_x}\int \psi_z \,\mathrm{d}x\right)^2 \mathrm{d}z = \frac{1}{2L_z}\int \bar{U}^2 \,\mathrm{d}z, \tag{3.2d}$$

$$K_{fluc} = K_{tot} - K_{jet}. \tag{3.2e}$$

Here L_x and L_z represent the domain size in the x and z directions, respectively, and $A = L_x L_z$ is the domain area. For the purposes of these definitions we speak of a jet whenever the horizontally averaged horizontal velocity $\bar{U}$ is non-zero. Although we refer here to P_S simply as a potential energy it is in fact the consumed available potential energy, defined for a weak salinity redistribution as the potential energy difference between the perturbed state and the unstably stratified background salinity field.

In this parameter regime the MRBC system exhibits remarkable relaxation oscillations that are also shared by the primitive equations (Garaud & Brummell 2015). After an initial transient, a statistically stationary state is achieved in which the four global quantities defined in (3.2) all oscillate with a well-defined period but fluctuate in amplitude. Figure 2(*e*) shows that the salinity potential energy P_S, salinity flux F_S and the fluctuation kinetic energy K_{fluc} all oscillate in phase but that the kinetic energy K_{jet} in the jets lags behind. The presence of very similar behaviour in both the primitive equations and the asymptotic MRBC system indicates that the latter is not missing any essential physics. We understand this behaviour as follows: efficient fingering, characterized by large salinity flux F_S, drives horizontal jets resulting in the growth of K_{jet}. The strengthening jets shear out the salt-finger field (Linden 1974; Smyth & Kimura 2007; Fernandes & Krishnamurti 2010; Radko 2010; Radko *et al.* 2015), resulting in an abrupt collapse of the fluctuations that feed the jets. As a result the jet starts to weaken, and when it is weak enough the fluctuations driven by the salinity stratification regrow and the jet starts to strengthen again. This process then repeats, leading to the observed relaxation oscillations (Garaud & Brummell 2015). A similar mechanism is responsible for relaxation oscillations in two-dimensional high-Ra, moderate-Pr Rayleigh–Bénard convection (Rucklidge & Matthews 1996; Fitzgerald & Farrell 2014; Goluskin *et al.* 2014), in three-dimensional Rayleigh–Bénard convection (Matthews *et al.* 1996) and in magnetoconvection (Rucklidge & Matthews 1996). In § 6 we use this idea to propose a phenomenological model of these relaxation oscillations in order to explain the observed Ra-dependence of the jet properties.

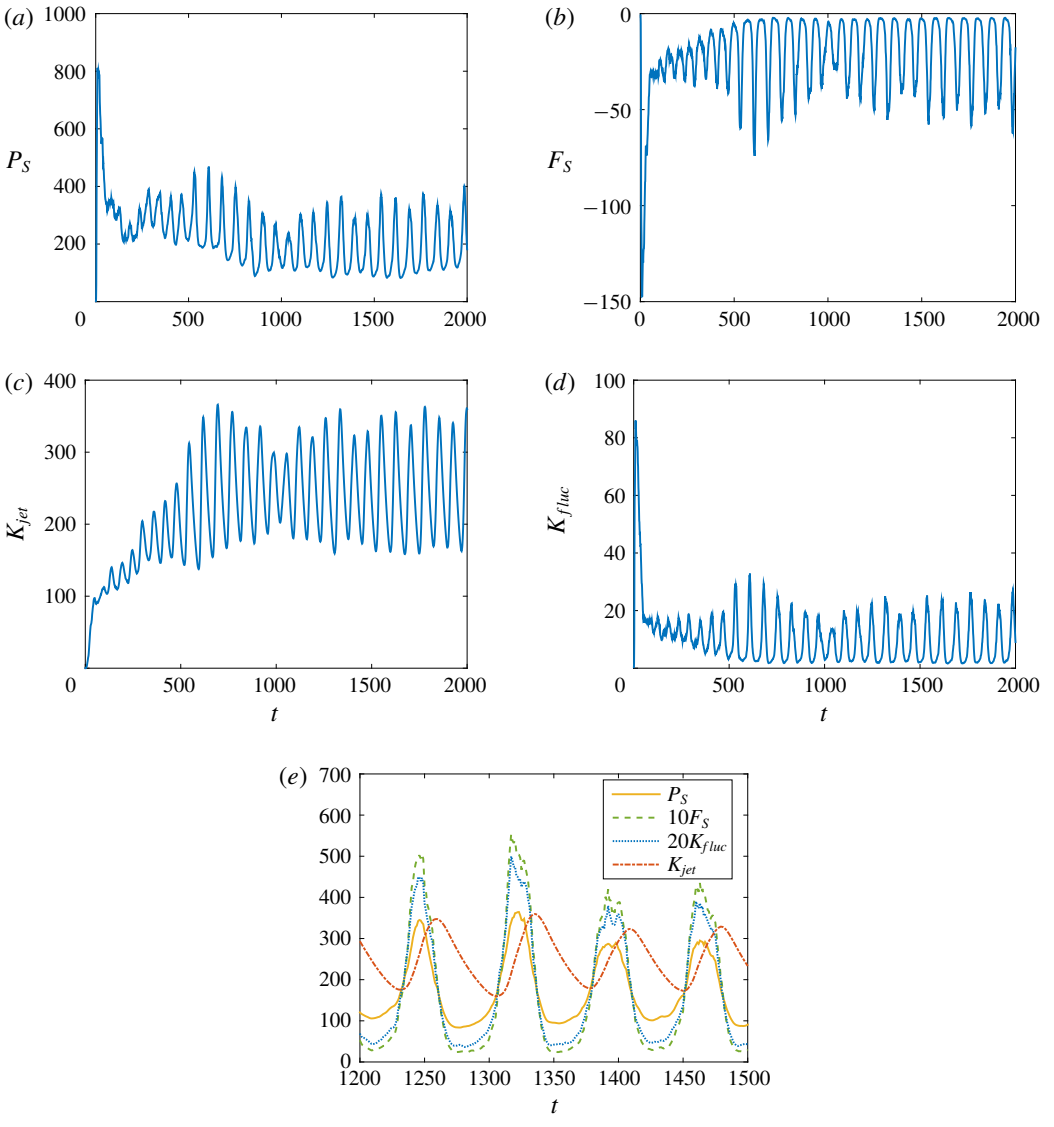

FIGURE 2. (Colour online) Evolution of salinity potential energy P_S, salinity flux F_S, kinetic energy K_{jet} in the jets and the fluctuation kinetic energy K_{fluc} in a doubly periodic domain of size $L_x \times L_z \equiv 32l_{opt} \times 32l_{opt}$ obtained from the MRBC equations (2.1) when $Ra = 6$ and $Sc = 1$. Panel (*e*) shows a comparison of phases of these quantities (suitably normalized) for $t \in [1200,\ 1500]$.

The evolution of the jets in time is shown in figure 3 in terms of a space–time Hovmöller plot of the horizontally averaged horizontal velocity $\bar{U}(z,\ t)$. The jets initially coarsen, but subsequently the coarsening process appears to terminate. Superposed on the jets are relaxation oscillations that are observed at all times after an initial transient. These oscillations are almost exactly in phase in all the jets, even though the jets are not all equally strong.

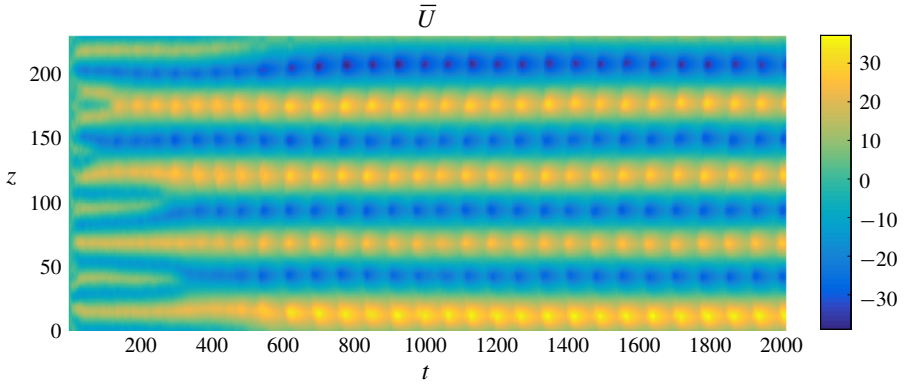

FIGURE 3. (Colour online) Space–time evolution of the jet profile $\bar{U}(z, t)$ in the MRBC system when $Ra = 6$ and $Sc = 1$.

3.2. *Simulation of the MRBC system with* $Ra = 2$, $Sc = 1$

In this section we show the corresponding results with $Ra = 2$ and $Sc = 1$ in a doubly periodic domain of the same effective size $L_x \times L_z = 32 l_{opt} \times 32 l_{opt}$, with l_{opt} now computed for $Ra = 2$. In this case the density ratio is three times larger and comparable to the inverse of the small diffusivity ratio. This parameter regime is hard to reach in DNS of the primitive equations describing salt-finger convection owing to the high buoyancy frequency associated with large density ratios (Garaud & Brummell 2015). However, the MRBC system (2.1) is quite capable of reaching this extreme parameter regime and at low cost.

In figure 4 we show the time evolution of the salinity potential energy P_S, salinity flux F_S, kinetic energy K_{jet} in the jets and the fluctuation kinetic energy K_{fluc}. We see that P_S, F_S and K_{fluc} equilibrate relatively quickly while the jet kinetic energy K_{jet} undergoes several step-like increases that correlate well with jet mergers (figure 5*a*). The resulting two-jet state persists for a long time, but not forever: if the calculation is continued to $\gtrsim 10^5$ (not shown) one finds that the two jets eventually also merge and the final state of the system therefore consists of a single jet to the right (accompanied, of course, by a similar jet to the left). Moreover, the relaxation oscillations that proved so dominant at $Ra = 6$ are now largely submerged in the fluctuation field.

Because of the longer time integration, $t = [0,\ 2.2 \times 10^4]$, as compared with that in § 3.1, we observe more coarsening events – the four jets coarsen into three around $t = 5000$ and then into two around $t = 14\,000$. The snapshots of the horizontal velocity field $u(x, z, t)$ (figure 5*b–e*) show that at the very initial time, the salt-finger distribution is almost uniform in height, with no hint of jet formation. However, as time proceeds, jets begin to form and strengthen as a result of repeated mergers. Figure 6 shows the corresponding snapshots of the salinity field S. The salt fingers are clearly visible in the initial stages of evolution but are subsequently shredded by the growing horizontal flow.

To describe the jets we define the dominant jet wavenumber

$$m_{dominant} = \frac{\int |m|^3 |\hat{\bar{\psi}}|^2 \, \mathrm{d}m}{\int |m|^2 |\hat{\bar{\psi}}|^2 \, \mathrm{d}m}, \tag{3.3}$$

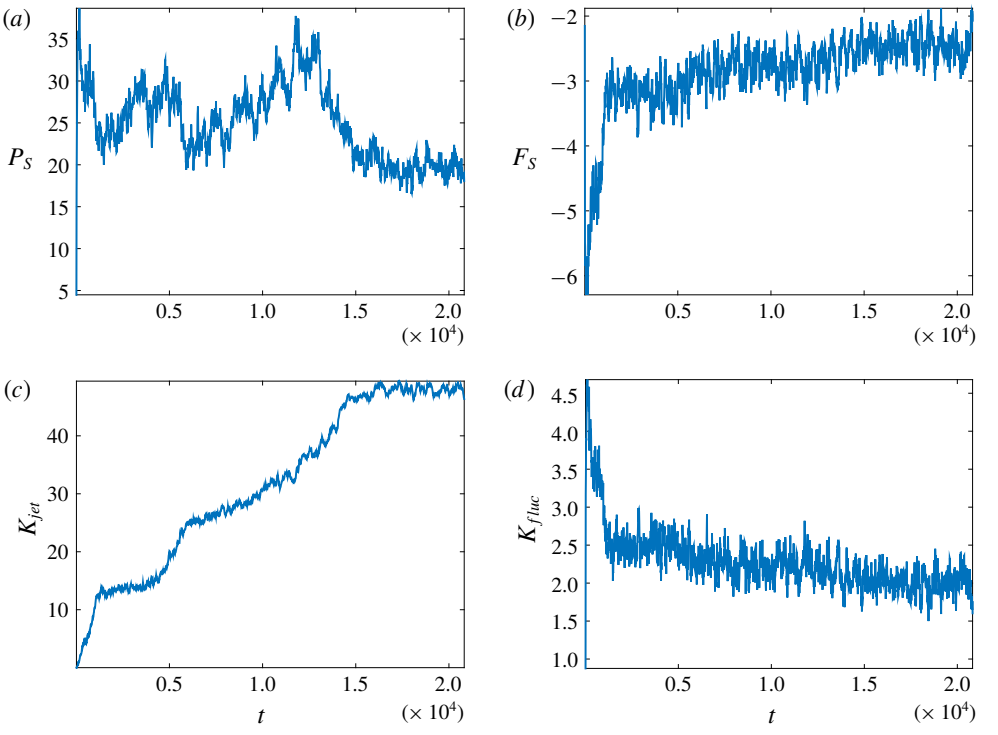

FIGURE 4. (Colour online) Evolution of salinity potential energy P_S, salinity flux F_S, kinetic energy K_{jet} in the jets and the fluctuation kinetic energy K_{fluc} in a doubly periodic domain of size $L_x \times L_z = 32l_{opt} \times 32l_{opt}$ obtained from the MRBC equations (2.1) when $Ra = 2$ and $Sc = 1$. A statistically stationary state is present for $t \gtrsim 1.5 \times 10^4$.

where $\hat{\bar{\psi}}$ is the Fourier transform of the horizontally averaged streamfunction $\bar{\psi}$. Figure 7 shows the dependence of the total kinetic energy on the dominant jet wavenumber during a simulation run, with the latter normalized by the wavenumber corresponding to the domain height. Thus, at the end of this simulation, $2\pi m/L_z$ reaches 2. We observe that as the system evolves, the dominant wavenumber decreases and the jet kinetic energy surpasses the fluctuation kinetic energy. In addition, we identify a scaling law for the total kinetic energy, $K_{tot} \sim m_{dominant}^{-\alpha}$ with $5/3 \lesssim \alpha \lesssim 2$, quantifying the growth in kinetic energy as the system coarsens.

To illuminate the details of this energy increase, we show in figure 8 the spectrum of the jet kinetic energy

$$E_{Kjet} = \tfrac{1}{2}m^2|\hat{\psi}(0, m)|^2 \tag{3.4}$$

at $t = 3000$, 8000 and 15 000, corresponding to states with 4, 3 and 2 jets, respectively (figure 5*a*). We observe that except on the largest scales, the jet kinetic energy spectrum exhibits a m^{-4} scaling, for which we provide an explanation in § 5. We can also identify a bulge in energy at the largest scale present and track it to yet larger scales as time progresses and the system coarsens. Throughout the paper, we use the notation E to denote spectra – for example, if K_{jet} is the domain-averaged jet kinetic energy then E_{Kjet} is the corresponding spectrum.

We next focus on gathering information about the dynamics and dominant balances in the MRBC system (2.1) in spectral space. For this purpose we observe that in

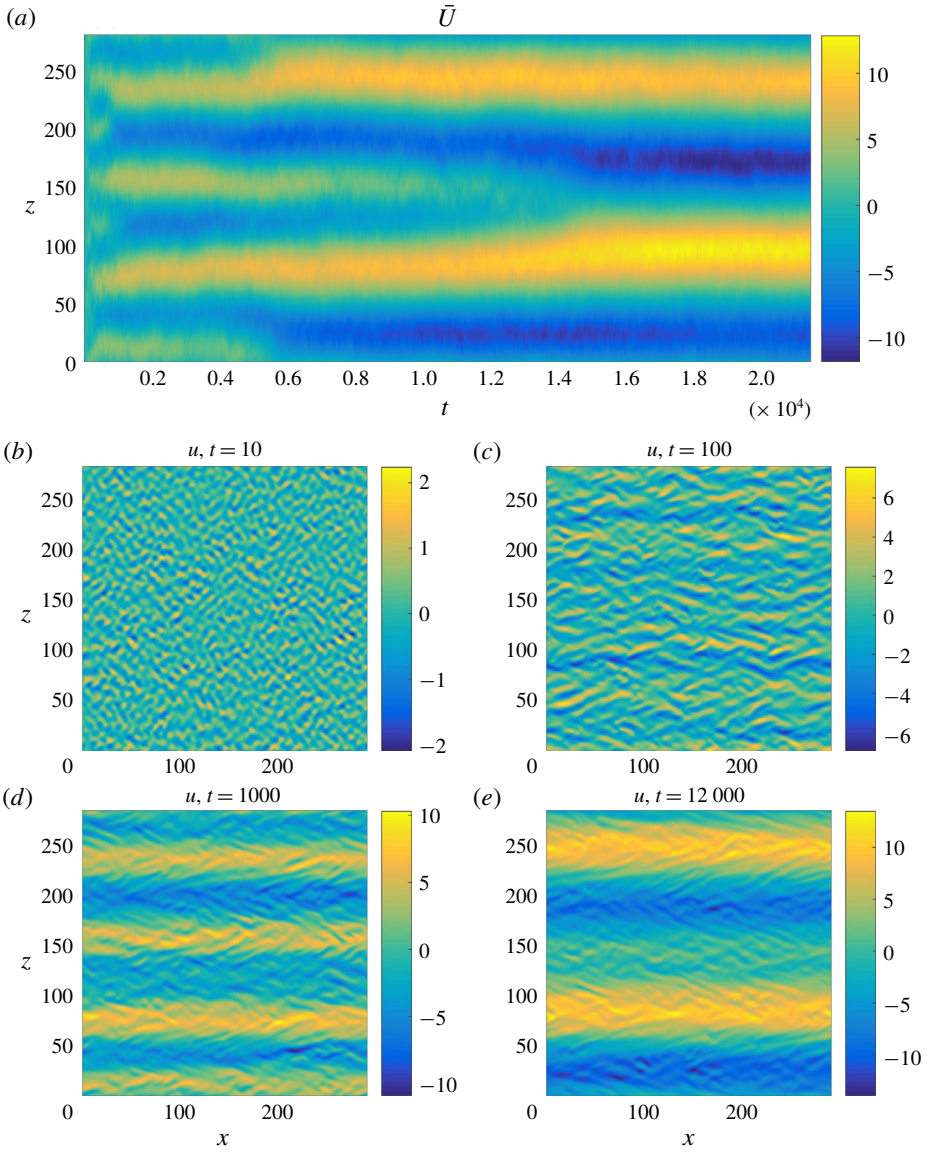

FIGURE 5. (Colour online) (*a*) Space–time evolution of the jet profile $\bar{U}(z, t)$ in the MRBC system when $Ra = 2$ and $Sc = 1$. (*b–e*) Snapshots of $u(x, z, t)$ at $t = 10$, 100, 1000 and 12 000, respectively.

spectral space

$$\frac{\mathrm{d}}{\mathrm{d}t}E_{Ktot} = T_\psi + F_\psi - Dl_\psi - Ds_\psi, \tag{3.5}$$

where

$$E_{Ktot} = \tfrac{1}{2}(k^2 + m^2)|\hat{\psi}(k, m)|^2, \tag{3.6a}$$

$$T_\psi = \tfrac{1}{2}(\hat{\psi}^* \widehat{\mathcal{J}(\psi, \nabla^2\psi)} + \text{c.c.}), \tag{3.6b}$$

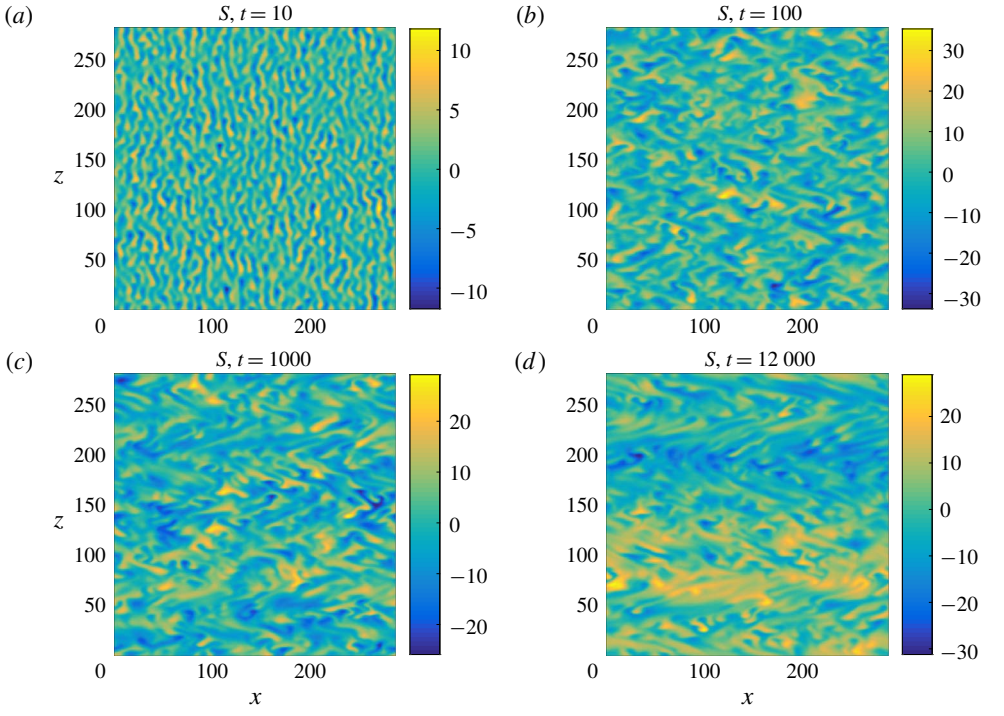

FIGURE 6. (Colour online) (*a–d*) Snapshots of $S(x, z, t)$ at $t = 10$, 100, 1000 and 12 000, respectively.

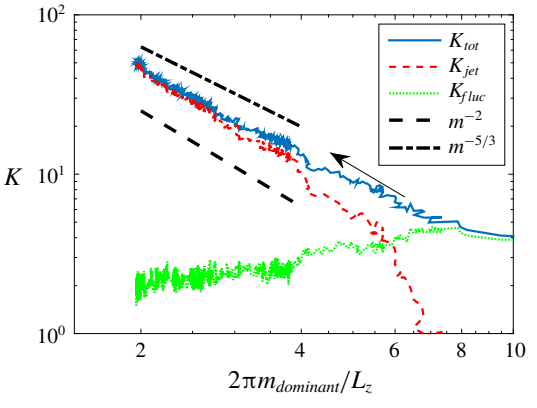

FIGURE 7. (Colour online) Dependence of the total kinetic energy K_{tot} (blue solid curve), the kinetic energy K_{jet} in the jets (red dashed curve) and the kinetic energy K_{fluc} in the fluctuations (green dotted curve) on the dominant jet wavenumber $m_{dominant}$. The black arrow indicates the direction of time evolution. The black dashed and dot-dashed lines represent m^{-2} and $m^{-5/3}$ relations, respectively, and are provided for visual guidance.

$$F_\psi = -\tfrac{1}{2}(\mathrm{i}k\hat{\psi}\hat{S}^* + \text{c.c.}), \tag{3.6c}$$

$$Dl_\psi = \frac{k^2}{k^2 + m^2}|\hat{\psi}(k, m)|^2, \tag{3.6d}$$

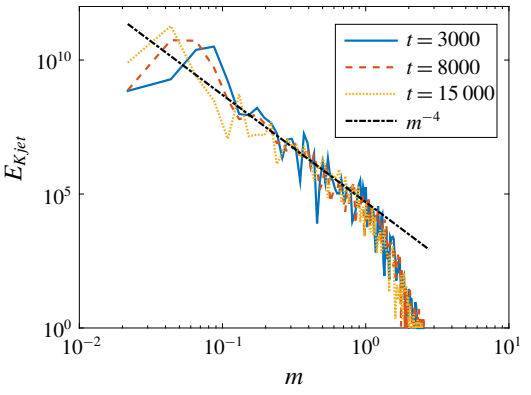

FIGURE 8. (Colour online) Jet kinetic energy spectrum at $t = 3000$, 8000 and 15 000. The black dot-dashed line represents the m^{-4} relation and is provided for visual guidance.

$$Ds_\psi \;=\; (k^2 + m^2)^2 |\hat{\psi}(k, m)|^2. \tag{3.6e}$$

Here the superscript * indicates a complex conjugate. Equation (3.5) describes the contributions to the evolution of E_{Ktot} arising from energy transport through advection (T_ψ) and buoyancy (F_ψ) together with energy losses via large-scale (Dl_ψ) and small-scale (Ds_ψ) dissipation. Next, we introduce a decomposition into a mean and a fluctuating part, $\psi = \bar{\psi} + \psi'$, and separate the fluctuation transport equation into mean–fluctuation and fluctuation–fluctuation contributions, defined as follows:

$$T_{\psi,m+f\to f} \;=\; \tfrac{1}{2}(\hat{\psi}'^{*}\widehat{(\psi'_x\bar{\psi}_{zzz} - \bar{\psi}_z\nabla^2\psi'_x)} + \text{c.c.}), \tag{3.7a}$$

$$T_{\psi,f+f\to f} \;=\; \tfrac{1}{2}(\hat{\psi}'^{*}\widehat{\mathcal{J}(\psi', \nabla^2\psi')} + \text{c.c.}). \tag{3.7b}$$

Thus $T_{\psi,f} = T_{\psi,m+f\to f} + T_{\psi,f+f\to f}$ is the total fluctuation transport.

We begin by focusing on the fluctuating component by subtracting the spectrum of the mean from the total spectrum, and define the fluctuation kinetic energy spectrum as $E_{Kfluc} = E_{Ktot} - E_{Kjet}$. In figure 9 we show the fluctuation spectrum E_{Kfluc} at $t = 10$, the initial stage of evolution. Figure 9(*a*) shows that the fluctuation kinetic energy initially centres on the optimal wavenumber for instability, much as in the IFSC regime in the limit $Sc \to \infty$. Comparison of panels (*b–d*) shows that advection is dominated by the fluctuation–fluctuation interaction, while the mean–fluctuation interaction is of higher order, as is made explicit by the colour difference in the associated colour maps. The transport of energy from small scales to large scales (inverse cascade) via the fluctuation–fluctuation interaction resembles that in 2D turbulence. This is illustrated in figure 9(*c*) by the extraction and injection of energy around the optimal wavenumber and marginal curve at $k = 0$, respectively.

When jets form, the dominant balance changes. In figure 10 we show the spectra of the various contributions to (3.5) at $t = 1000$. The fluctuation kinetic energy spectrum no longer concentrates around the optimal wavenumber, but now centres around the marginal curve at $k \approx 0$. In addition, as evidenced by the differing range of scale in the colour maps, the dominant component in energy transport is now the mean–fluctuation interaction instead of the fluctuation–fluctuation interaction. We will make use of this important observation in the next section.

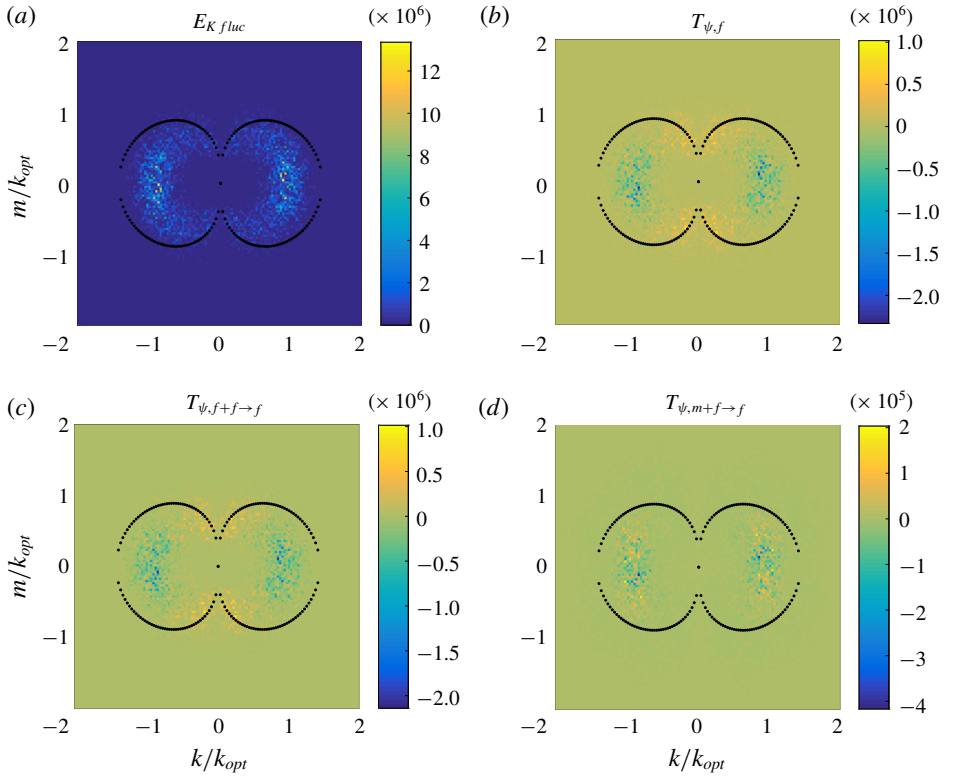

FIGURE 9. (Colour online) Spectra of (*a*) the fluctuation kinetic energy E_{Kfluc}, (*b*) energy transport $T_{\psi,f}$, (*c*) fluctuation–fluctuation interaction $T_{\psi,f+f\to f}$ and (*d*) the mean–fluctuation interaction $T_{\psi,m+f\to f}$ at $t = 10$, computed from the MRBC system (2.1) with $Ra = 2$ and $Sc = 1$. The black dots mark the marginal curve for linear instability.

The direction of transport is revealed in figure 11, which shows the spectra of the various contributions to (3.5) averaged over $t = [9000,\ 12\,000]$, a time interval corresponding to the presence of three jets. The fluctuation kinetic energy spectrum E_{Kfluc} centres around the marginal curve and transport is dominated by the mean–fluctuation interactions. The latter transport energy from small to large scales along the marginal curve, while the mean–fluctuation interaction transports energy mostly across the marginal curve.

We can obtain an analogous description of salinity transport in spectral space. Multiplying (2.1*a*) by $\hat{S}^*$ and adding the complex conjugate leads to the potential energy equation

$$\frac{\mathrm{d}}{\mathrm{d}t}E_S = T_S + F_S - D_S, \tag{3.8}$$

where

$$E_S = \tfrac{1}{2}|\hat{S}(k,m)|^2, \tag{3.9a}$$

$$T_S = \tfrac{1}{2}(\hat{\psi}^*\widehat{\mathcal{J}(\psi,S)} + \text{c.c.}), \tag{3.9b}$$

$$F_S = +\tfrac{1}{2}(\mathrm{i}k\hat{\psi}\hat{S}^* + \text{c.c.}) = -F_\psi, \tag{3.9c}$$

$$D_S = (k^2+m^2)|\hat{S}(k,m)|^2. \tag{3.9d}$$

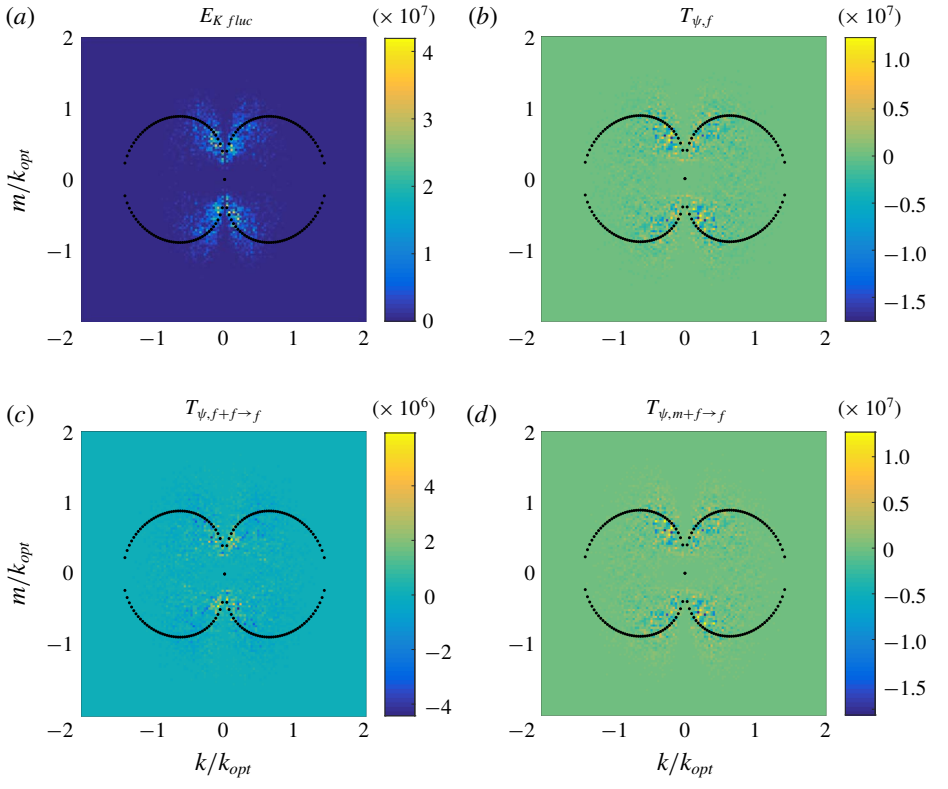

FIGURE 10. (Colour online) Spectra of (*a*) the fluctuation kinetic energy E_{Kfluc}, (*b*) energy transport $T_{\psi,f}$, (*c*) fluctuation–fluctuation interaction $T_{\psi,f+f\to f}$ and (*d*) the mean–fluctuation interaction $T_{\psi,m+f\to f}$ at $t=1000$, computed from the MRBC system (2.1) with $Ra=2$ and $Sc=1$. The black dots mark the marginal curve for linear instability.

As before, we define the jet and fluctuation parts of the salinity potential energy spectrum

$$E_{Sjet} = \tfrac{1}{2}|\hat{S}(0,m)|^2, \tag{3.10a}$$

$$E_{Sfluc} = E_S - E_{Sjet}, \tag{3.10b}$$

and the mean–fluctuation and fluctuation–fluctuation transports:

$$T_{S,m+f\to f} = \tfrac{1}{2}(S'^*\widehat{(\psi'_x\bar{S}_z - S'_x\bar{\psi}_z)} + \text{c.c.}), \tag{3.11a}$$

$$T_{S,f+f\to f} = \tfrac{1}{2}(S'^*\widehat{\mathcal{J}(\psi',S')} + \text{c.c.}), \tag{3.11b}$$

$$T_{S,f} = T_{S,m+f\to f} + T_{S,f+f\to f}. \tag{3.11c}$$

Figure 12 shows E_{Sfluc} and $T_{S,f}$ averaged over $t=[9000,\ 12\,000]$. The salinity field differs from the streamfunction by its concentration at large scale both horizontally and vertically.

To understand the mean balance, we take the time and horizontal (zonal) average over a statistically steady state of the MRBC system (2.1). We obtain

$$\frac{1}{Sc}\overline{\psi_x\psi_z} = \bar{\psi}_{zz}, \tag{3.12a}$$

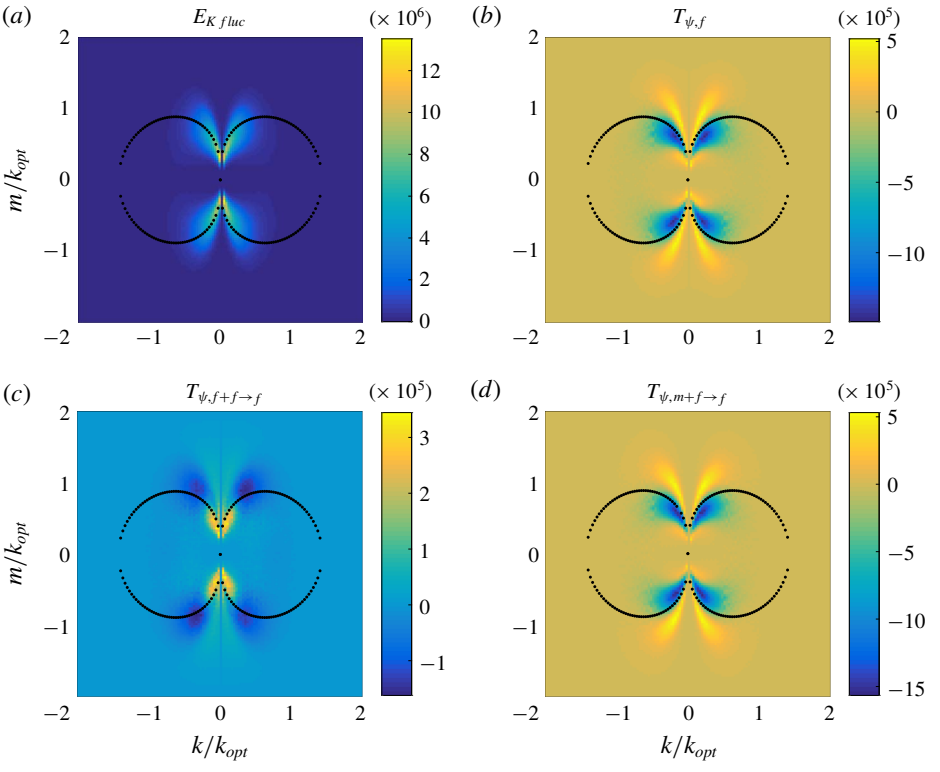

FIGURE 11. (Colour online) Spectra of (*a*) the fluctuation kinetic energy E_{Kfluc}, (*b*) the energy transport $T_{\psi,f} \equiv T_{\psi,f+f\to f} + T_{\psi,m+f\to f}$, and its decomposition into (*c*) the fluctuation–fluctuation interaction $T_{\psi,f+f\to f}$ and (*d*) the mean–fluctuation interaction $T_{\psi,m+f\to f}$ averaged over $t = [9000,\ 12\,000]$, as computed from the MRBC system (2.1) with $Ra = 2$ and $Sc = 1$. The black dots mark the marginal curve for linear instability.

$$\overline{\psi_x S} = \bar{S}_z + \text{const.}, \tag{3.12b}$$

a result confirmed in figure 13, indicating that the system has reached a statistically steady state in which the jet structure is in balance with dissipation. In (3.12*b*) the constant of integration corresponds to the total downward salinity flux that drives the system by transferring available potential energy in the salinity field into kinetic energy, and hence must be non-zero. In contrast, equation (3.12*a*) contains no integration constant because the $x \to -x$ symmetry of the MRBC model prohibits shear with a preferred direction. The small differences between the left- and right-hand sides of (3.12) seen in figure 13 are a consequence of the slow coarsening process.

4. Further reduction

In the previous section we found that horizontal jets are the dominant structures in the MRBC system (2.1) at late times and that in the jet regime the mean–fluctuation interaction is stronger than the fluctuation–fluctuation interaction. In this section we make use of these findings to obtain two further simplifications of the MRBC system that continue to retain the essential dynamics of this system. These are the quasilinear

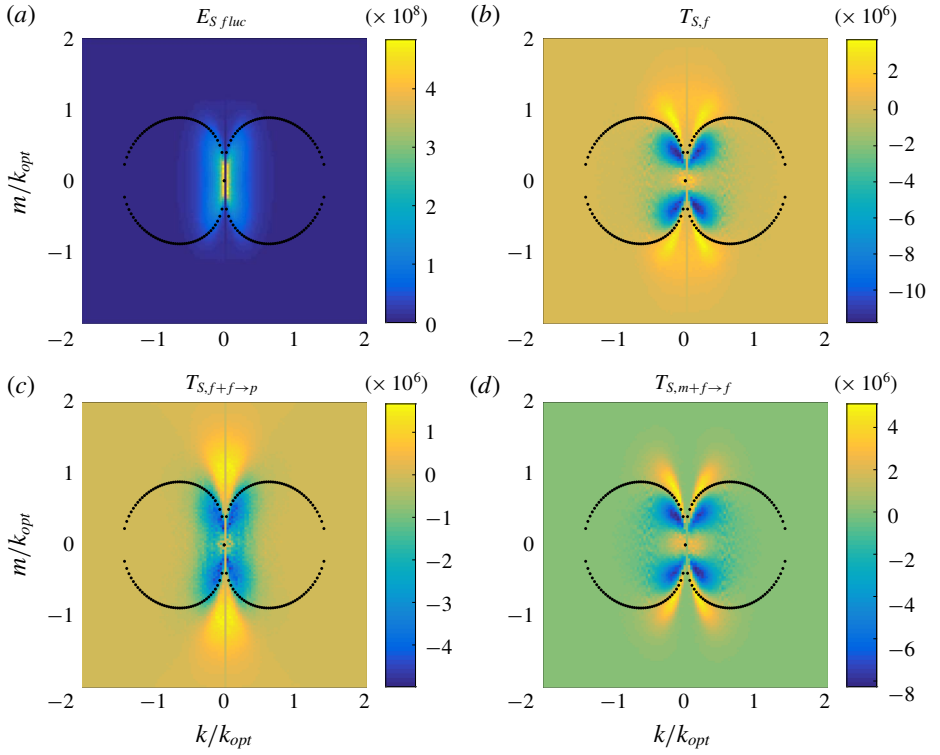

FIGURE 12. (Colour online) Spectra of (*a*) the fluctuation salinity potential energy E_{Sfluc}, (*b*) the salinity transport $T_{S,f} \equiv T_{S,f+f\to f} + T_{S,m+f\to f}$ and its decomposition into (*c*) the fluctuation–fluctuation interaction $T_{S,f+f\to f}$ and (*d*) the mean–fluctuation interaction $T_{S,m+f\to f}$ averaged over $t = [9000,\ 12\,000]$, as computed from the MRBC system (2.1) with $Ra = 2$ and $Sc = 1$. The black dots mark the marginal curve for linear instability.

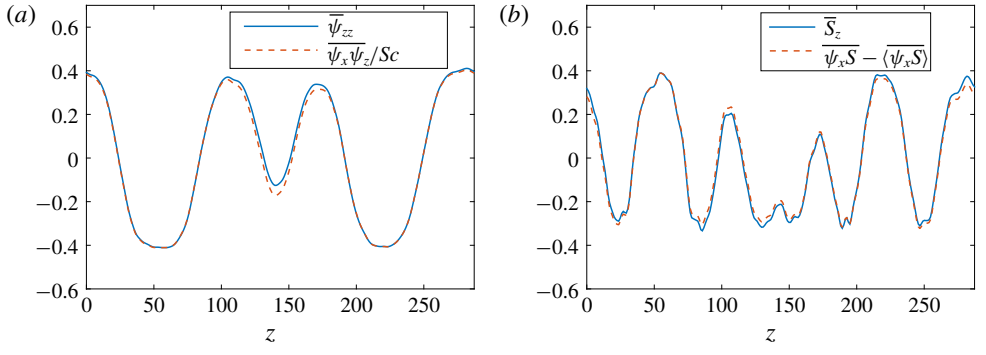

FIGURE 13. (Colour online) Contributions to the balance equations (3.12) for the MRBC system (2.1) with $Ra = 2$ and $Sc = 1$, time-averaged over $t = [9000,\ 12\,000]$. (*a*) Mean ψ balance. (*b*) Mean S balance.

system studied in § 4.1, obtained by neglecting the fluctuation–fluctuation interaction, and the single-mode system studied in § 4.2, with only one horizontal wavenumber. The results show that these two further reductions do, at least qualitatively, capture the

phenomena of jet formation and coarsening, and provide us with additional confidence in the phenomenological theory described in § 5.

4.1. *Quasilinear system*

In this section, we present the study of the quasilinear system obtained by neglecting the fluctuation–fluctuation interaction in the MRBC system (2.1). Mathematically, we replace the nonlinear advection terms by their quasilinear approximation:

$$\mathcal{J}(a, b) \to \mathcal{J}(\bar{a}, b') + \mathcal{J}(a', \bar{b}), \tag{4.1}$$

where a and b are arbitrary fields. Thus the mean–perturbation interaction contains both the mean-advected perturbation field and the perturbation-advected mean field. This approximation has been widely used in studies of jet formation on the β-plane with random forcing (cf. Farrell & Ioannou 2003, 2007; O'Gorman & Schneider 2007; Marston, Conover & Schneider 2008; Srinivasan & Young 2012) because it leads to a relatively simple description of the statistical properties of the solution in terms of cumulants. However, the quasilinear approximation may apply to deterministic systems as well. In some cases the approximation may be justified by appropriate asymptotic analysis (Beaume *et al.* 2015), but here it is made on the basis of our numerical observations. We show below that the mean–fluctuation interaction alone can generate and maintain horizontal jets, without the presence of an inverse cascade mechanism due to the fluctuation–fluctuation interaction. For this study we therefore retain the parameters $Ra = 2$ and $Sc = 1$ and likewise retain the domain size and resolution of the previous section, unless otherwise specified.

Numerical integration of the resulting quasilinear system shows that all quantities settle into a statistically steady state, although here they do so much faster than the corresponding quantities in figure 4. In figure 14 we compare the time evolution of the salinity potential energy P_S, salinity flux F_S, and the kinetic energy K_{jet} and K_{fluc} of the jets and the associated fluctuations in the quasilinear system (blue curves) with the corresponding results from the MRBC model (red curves). The figure shows that the salinity potential energy and the fluctuation kinetic energy in the saturated state are larger than those in the MRBC system, while the salinity flux and the jet kinetic energy are weaker. However, a more careful look reveals that the jet kinetic energy in the quasilinear linear system saturates at approximately the same level as the initial saturation level in the MRBC system, although subsequent coarsening in the latter leads to growing divergence between the two. At the same time the coarsening in the MRBC system leads to growing convergence with the salinity potential energy in the quasilinear system. Figure 15 shows a typical evolution of the horizontally averaged horizontal velocity as well as snapshots of the instantaneous horizontal velocity $u(x, z, t)$. The key feature we observe is that jets still form, indicating that the primary mechanism behind jet formation is the mean–fluctuation interaction. As in the full system, we observe that initially narrow jets gradually coarsen into fewer broader and more energetic jets, although here the three-jet state appears to be more stable and persists for a longer time than in the MRBC system. However, the structure of the fluctuating horizontal velocity field $u(x, z, t)$ differs in detail from that of the MRBC system (figure 5), with small horizontal scale structures suppressed and replaced over time by prominent V-shaped structures that stretch across the domain in the horizontal direction (figure 15*b–e*).

Figure 16 shows the corresponding snapshots of the salinity field $S(x, z, t)$, whose behaviour also resembles that of the full MRBC system (figure 6) – as the mean velocity field strengthens with time, it shears the salt fingers more efficiently and we observe smaller-scale fingers. These are gradually submerged into horizontal

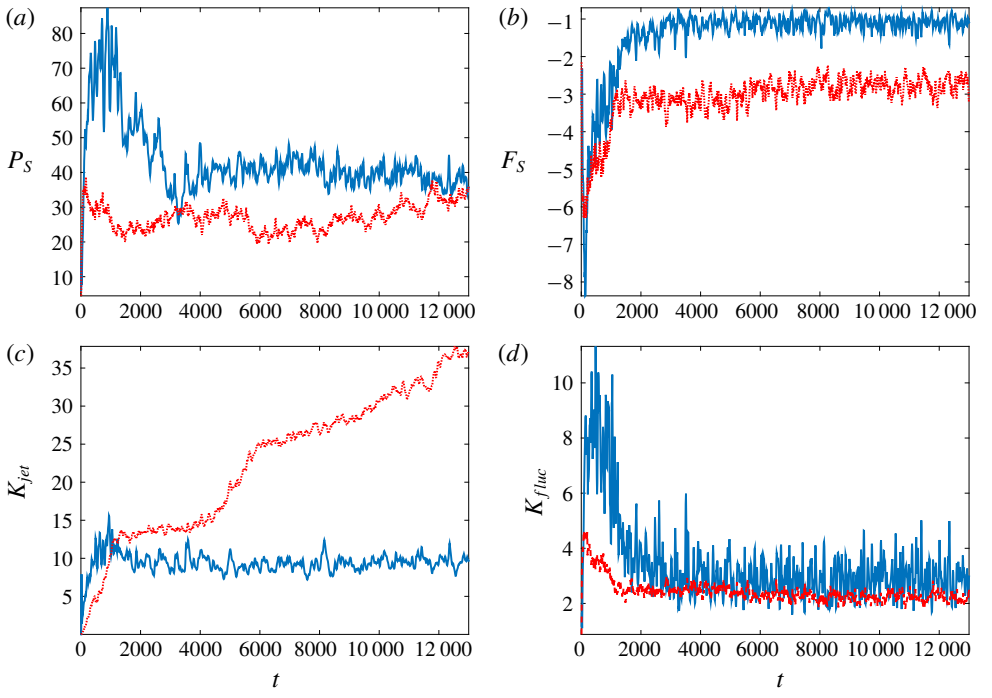

FIGURE 14. (Colour online) Blue solid curves: evolution of the salinity potential energy P_S, salinity flux F_S, the jet kinetic energy K_{jet} and the kinetic energy K_{fluc} of the associated fluctuations computed from the quasilinear system with $Ra = 2$ and $Sc = 1$ in a doubly periodic domain of size $L_x \times L_z = 32l_{opt} \times 32l_{opt}$. Red dashed curves: corresponding quantities from the MRBC system (shown in figure 4).

domain-size structures reflecting similar structures in the $u(x, z, t)$ snapshots. Qualitatively similar results were obtained for moderately low Prandtl numbers by Radko (2010) using a weakly nonlinear mean-field approach.

We conclude this subsection with figure 17, showing the spectrum of the fluctuation kinetic energy E_{Kfluc} and the transport term T_ψ averaged over $t = [10\,000,\ 11\,000]$. The figure shows that the fluctuation kinetic energy concentrates at the horizontal wavenumber corresponding to the domain size while centring around the marginal curve. These large horizontal scale structures are particularly prominent in figure 15(*e*). From the transport term shown in figure 17(*b*) we see that advection transports energy from linearly growing modes to linearly damped modes, much as occurs in the full MRBC system.

4.2. *Single-mode system*

In the previous section we found that the quasilinear system can successfully generate jets and that energy concentrates at the largest horizontal scales accessible to the system. In this section we use this information to reduce the quasilinear system yet further, to a single-mode system with only one horizontal wavenumber corresponding to the domain size, $k = \pi/(16l_{opt})$, retained in the fluctuation field. As before we present results from this procedure for the parameters $Ra = 2$ and $Sc = 1$.

Figure 18 shows the time evolution of the salinity potential energy P_S, salinity flux F_S, kinetic energy K_{jet} in the jets and the kinetic energy K_{fluc} in the associated

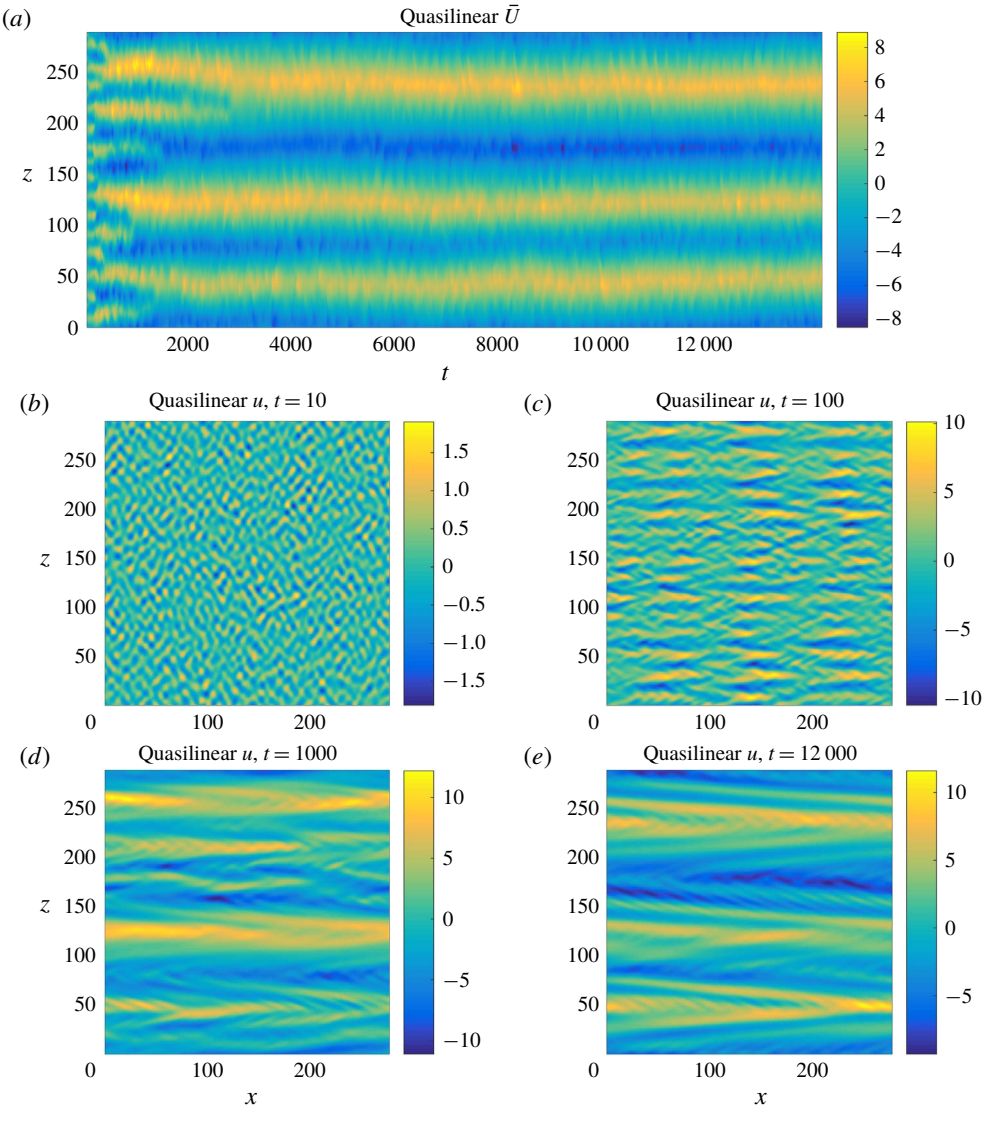

FIGURE 15. (Colour online) (*a*) Space–time evolution of the jet profile $\bar{U}(z, t)$ in the quasilinear system when $Ra = 2$ and $Sc = 1$. (*b–e*) Snapshots of $u(x, z, t)$ at $t =$ 10, 100, 1000 and 12 000, respectively.

fluctuations and compares it with the evolution of the corresponding quantities in the MRBC system. As in the quasilinear system, the single-mode system also shows an initial energy peak, but this time the 'final' state is not as steady and bursts appear in the energy evolution. This abrupt bursting behaviour is also observed in the evolution of the jet state shown in figure 19. The main distinguishing feature of the single-mode system is that the jet coarsens to the domain size very quickly, but the subsequent properties of the jet structure are qualitatively similar to those found in both the quasilinear system and the MRBC system. Indeed, figure 18 shows that the salinity potential energy and the fluctuation kinetic energy are reproduced almost perfectly, although the salinity flux and the jet kinetic energy are in general weaker.

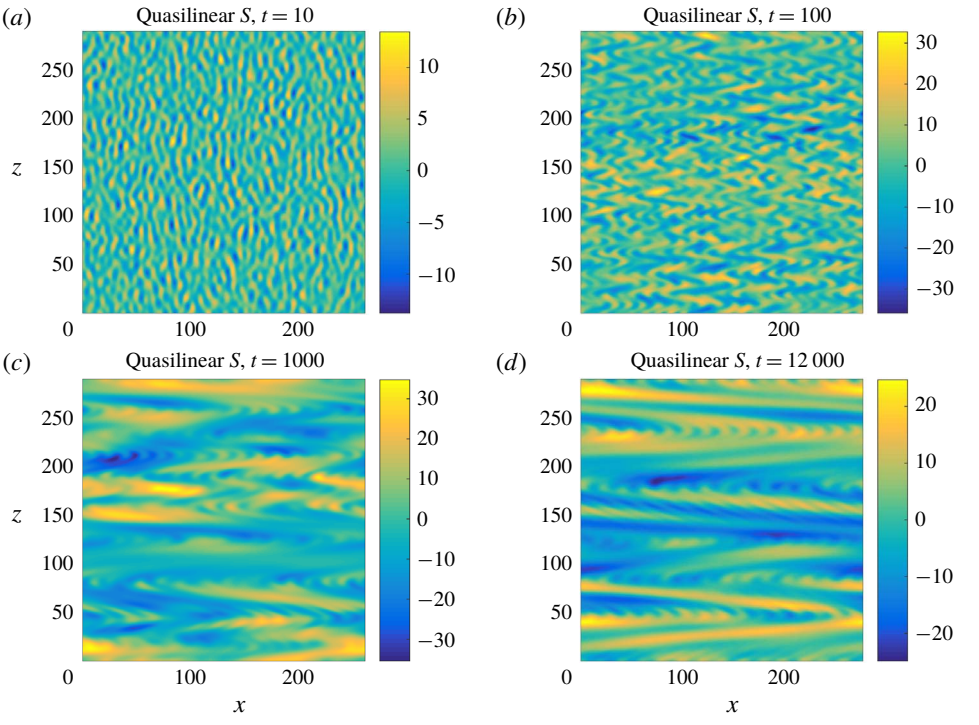

FIGURE 16. (Colour online) (*a–d*) Snapshots of $S(x, z, t)$ at $t = 10$, 100, 1000 and 12 000, respectively, for the quasilinear system with $Ra = 2$, $Sc = 1$.

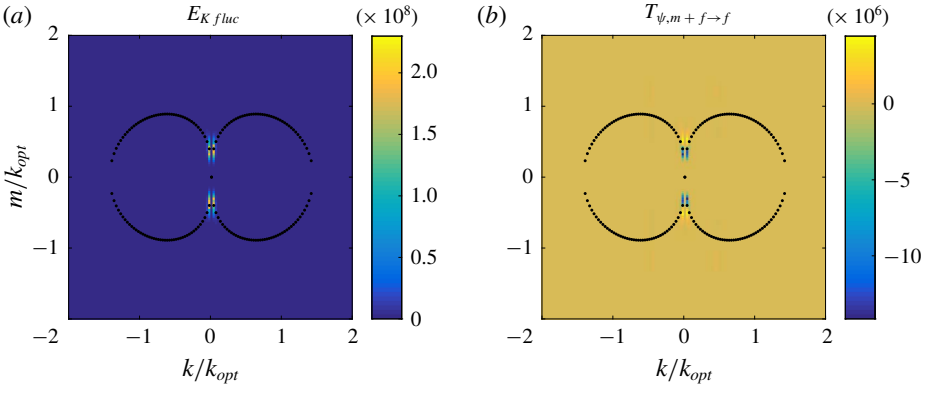

FIGURE 17. (Colour online) (*a*,*b*) Spectra of the fluctuation kinetic energy E_{Kfluc} and energy transport $T_{\psi,f}$ in the quasilinear system arising from the mean–fluctuation interaction, averaged over $t = [10\,000,\ 11\,000]$. The black dots mark the marginal curve for linear instability.

5. Spectra

In the previous section we showed that the quasilinear and single-mode models capture the essential behaviour of the MRBC model – jet formation and coarsening

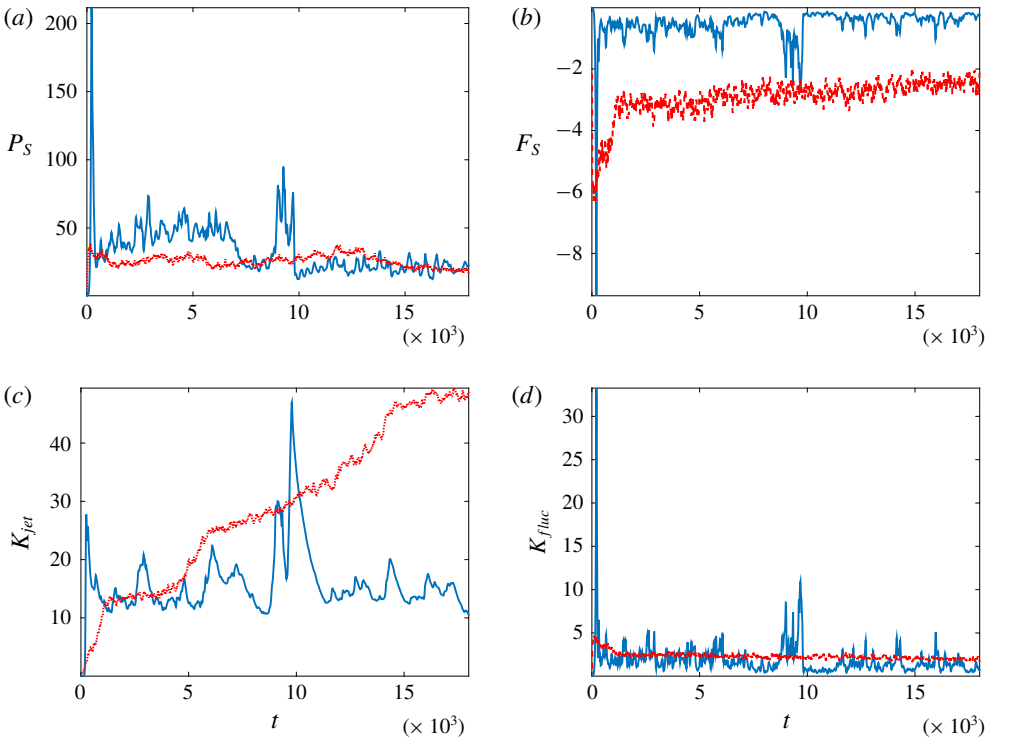

FIGURE 18. (Colour online) Blue solid curves: evolution of the salinity potential energy P_S, salinity flux F_S, the jet kinetic energy K_{jet} and the kinetic energy K_{fluc} of the associated fluctuations computed from the single-mode system with $Ra = 2$ and $Sc = 1$ and wavenumber $k = \pi/(16l_{opt})$ in a doubly periodic domain of size $L_x \times L_z = 32l_{opt} \times 32l_{opt}$. Red dashed curves: corresponding quantities from the MRBC system (shown in figure 4).

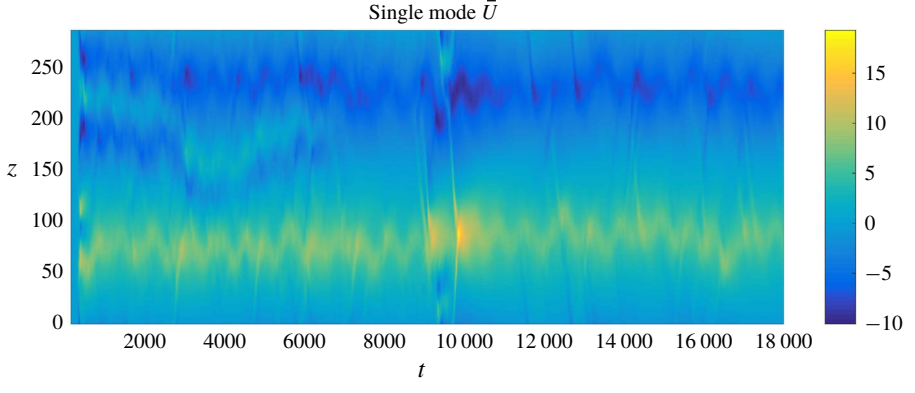

FIGURE 19. (Colour online) Space–time evolution of the jet profile $\bar{U}(z, t)$ in the single-mode system with $Ra = 2$ and $Sc = 1$ and wavenumber $k = \pi/(16l_{opt})$.

– despite differences in the detailed properties of the solutions. In this section we perform a more quantitative comparison by comparing and contrasting in detail the spectra of the solutions to the MRBC model and the quasilinear and single-mode approximations to it.

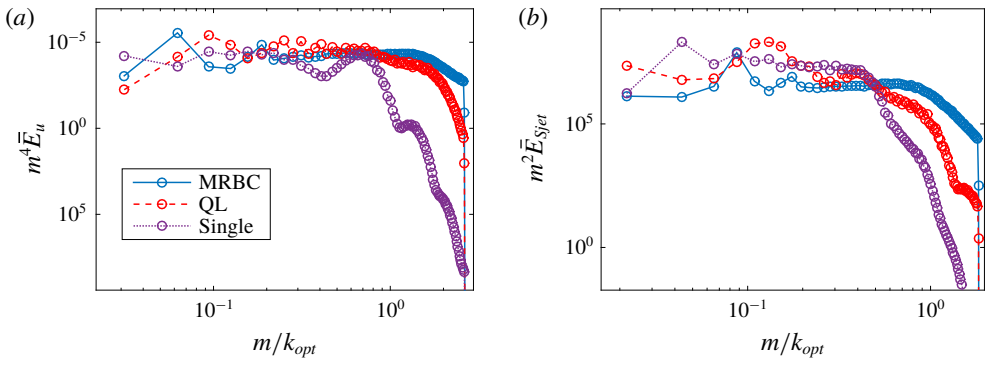

FIGURE 20. (Colour online) Compensated spectra of (*a*) the mean velocity and (*b*) the mean salinity for the MRBC model, the quasilinear (QL) model and the single-mode model with wavenumber $k = \pi/(16 l_{opt})$.

Figure 20 shows that all three systems exhibit the same zonal velocity spectrum $\bar{E}_u(m) = |\hat{u}(k=0, m)|^2/2 \sim m^{-4}$ and the same mean salinity spectrum $\bar{E}_{Sjet}(m) = |\hat{S}(k=0, m)|^2/2 \sim m^{-2}$ at sufficiently small m/k_{opt}. In view of our reduction procedure, this robust scaling must be a consequence of the mean–fluctuation interaction and insensitive to the fluctuation–fluctuation interactions. In fact, the fluctuation–fluctuation interactions are important only for wavenumbers $m/k_{opt} \gtrsim 0.7$. We emphasize that this scaling differs from the m^{-5} scaling for the planetary (β-plane) jet based on the Rossby wave dispersion relation (Rhines 1975).

To understand the origin of these large-scale spectral scalings we examine the dominant balances in the governing equations in spectral space. However, finding these balances in the MRBC and quasilinear models is not simple, owing to the k dependence of the terms. Figures 21 and 22 show the m dependence of $E_\psi = |\hat{\psi}|^2/2$ and $E_S = |\hat{S}|^2/2$ for fixed horizontal wavenumbers $k = 2\pi n_k/L_x$, $n_k = 1, 2 \ldots$, computed from the MRBC and quasilinear models, respectively. We see that while the spectrum of E_ψ does depend on k, the m-dependence of E_S is almost independent of k. Note that in these figures the quantities marked 'averaged' correspond to averaging over all the horizontal wavenumbers k, and not only over the five smallest wavenumbers shown in the plots.

The situation is simpler in the single-mode case. Figure 23 shows the spectra of the different contributions to the fluctuation momentum and fluctuation salinity balance in spectral space ((3.5) and (3.8)) as computed from the single-mode system in a statistically steady state when $Ra = 2$ and $Sc = 1$. We find that in the large-scale regime (small m) all quantities exhibit power-law behaviour. The dominant balance in the momentum equation is between energy pumping by buoyancy F_ψ and large-scale damping Dl_ψ; the slight imbalance between the two quantifies the contribution of the transport term T_ψ. In the salinity equation, the flux F_S, damping D_S and the transport term T_S are all comparable and in balance.

Figure 24 shows the spectrum of the transport term T_ψ in the momentum equation. This term consists of two contributions

$$T_{\psi 1} = \tfrac{1}{2}(\hat{\psi}^* \widehat{\bar{\psi}_z \nabla^2 \psi'_x} + \text{c.c.}) \quad \text{and} \quad T_{\psi 2} = \tfrac{1}{2}(\hat{\psi}^* \widehat{\psi'_x \bar{\psi}_{zzz}} + \text{c.c.}). \tag{5.1a,b}$$

Of these $T_{\psi 1}$ is the dominant term, while $T_{\psi 2}$ has the opposite sign and therefore reduces (slightly) the overall effectiveness of the first term.

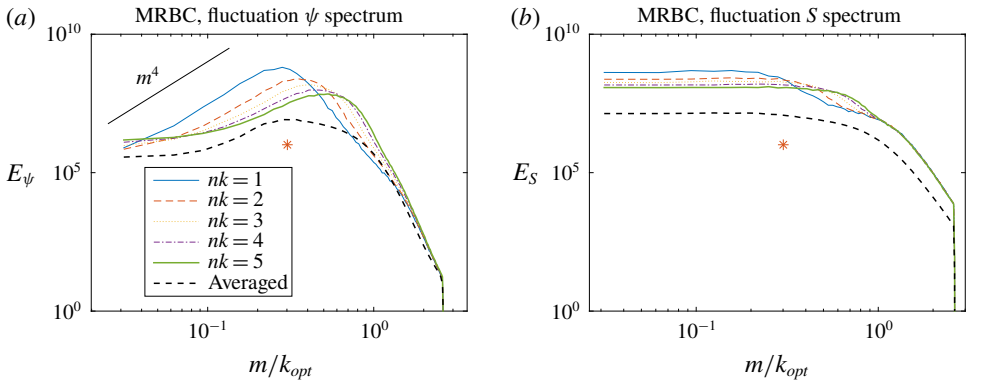

FIGURE 21. (Colour online) The quantities E_ψ and E_S at differing fixed horizontal wavenumbers k computed from the MRBC system with $Ra = 2$, $Sc = 1$. The black curve shows the spectrum obtained by averaging over k. The red star is the marginal vertical wavenumber corresponding to the smallest horizontal wavenumber $2\pi/L_x$. (*a*) MRBC, fluctuation ψ spectrum. (*b*) MRBC, fluctuation S spectrum.

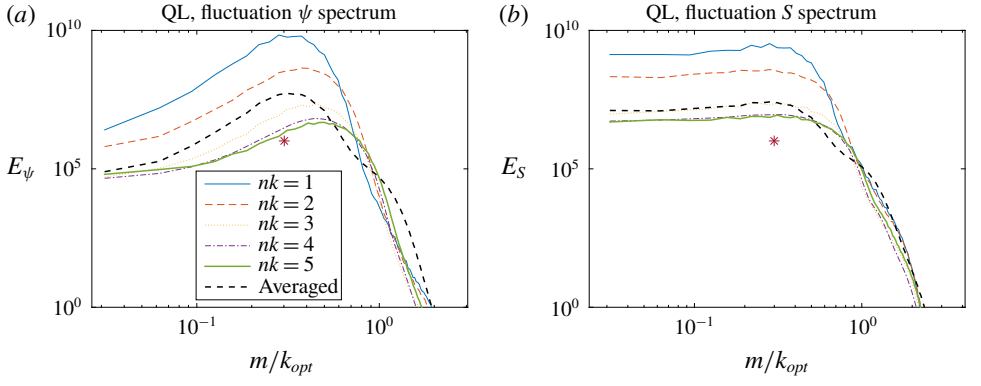

FIGURE 22. (Colour online) The quantities E_ψ and E_S at different fixed horizontal wavenumbers k computed from the quasilinear system with $Ra = 2$, $Sc = 1$. The black curve shows the spectrum obtained by averaging over k. The red star is the marginal vertical wavenumber corresponding to the smallest horizontal wavenumber $2\pi/L_x$. (*a*) QL, fluctuation ψ spectrum. (*b*) QL, fluctuation S spectrum.

We can express the above leading- and next-order balances in the ψ fluctuation equation as

$$F_\psi \sim Dl_\psi, \tag{5.2a}$$

$$T_{\psi 1} \sim Dl_\psi + F_\psi, \tag{5.2b}$$

approximating T_ψ by the dominant $T_{\psi 1}$ term. It is hard to estimate $Dl_\psi + F_\psi$, but our numerical results (figure 23) suggest that $Dl_\psi + F_\psi \sim mDl_\psi$. Since in the single-mode model $k \leqslant m \ll 1$ for large-scale modes in the vertical we approximate the Laplacian as $\Delta \sim m^{-2}$. The balances (5.2) then imply

$$\hat{S}' \sim \frac{1}{m^2}\hat{\psi}', \tag{5.3a}$$

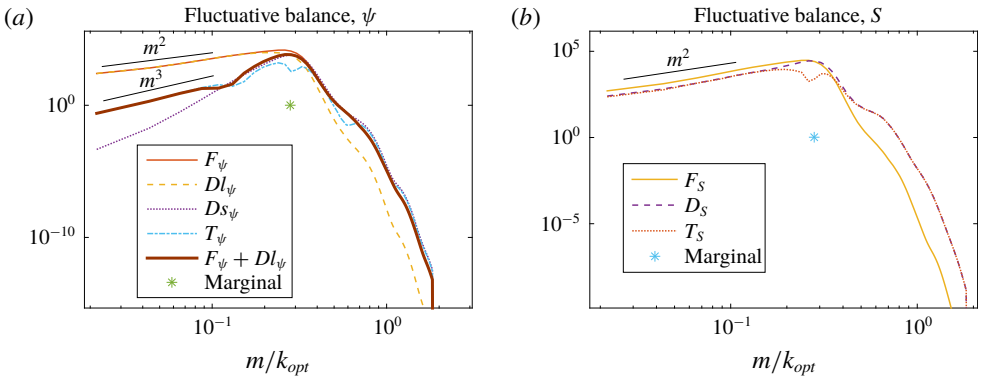

FIGURE 23. (Colour online) Contributions to (*a*) fluctuating momentum balance and (*b*) fluctuating salinity balance, in spectral space, obtained from the single-mode model with $Ra = 2$, $Sc = 1$ and wavenumber $k = \pi/(16 l_{opt})$. The star is the marginal vertical wavenumber corresponding to $k = \pi/(16 l_{opt})$.

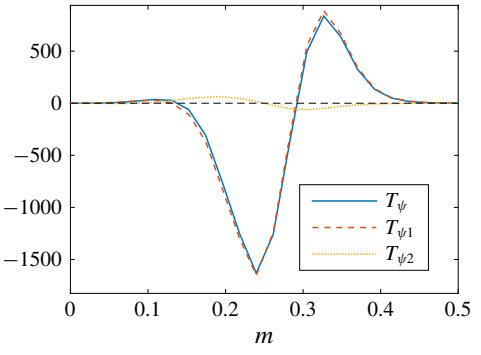

FIGURE 24. (Colour online) Transport terms in spectral space computed from the single-mode model with $Ra = 2$, $Sc = 1$ and wavenumber $k = \pi/(16 l_{opt})$.

$$\widehat{\bar{\psi}_z \nabla^2 \psi'_x} \sim m \frac{1}{m^2} \hat{\psi}'. \tag{5.3b}$$

To obtain a closed system we need the mean balance (3.12), which in spectral space can be written as

$$\widehat{\psi'_z \psi'_x} \sim m^2 \hat{\bar{\psi}}, \tag{5.4a}$$

$$\widehat{\psi'_x S'} \sim m \hat{\bar{S}}. \tag{5.4b}$$

To solve the closed system (5.3)–(5.4) we must compute the convolution integrals. These do not have a suitable asymptotic expansion valid in our large-scale regime, and we therefore calculate them numerically. For this purpose we assume that all quantities are described by piecewise power laws, i.e.

$$\hat{f}(m) = \begin{cases} |m|^{\alpha}, & |m| < m_0, \\ |m|^{\beta}, & |m| \geqslant m_0, \end{cases} \tag{5.5}$$

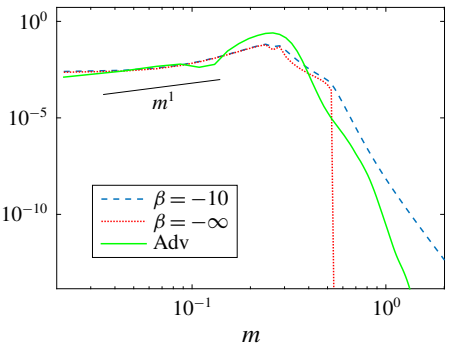

FIGURE 25. (Colour online) Numerical (green solid curve) and theoretical estimates of the left-hand side of (5.3*b*). The theoretical estimates use different values of the small-scale exponent β: blue curve for $\beta = -10$ and red curve for $\beta = -\infty$.

where m_0 denotes the transition between large and small scales. We also assume that the transition between these two regimes occurs at the marginal wavenumber, $m_0 = m_{mar} = (Ra-1)^{1/6}k^{1/3} = (Ra-1)^{1/6}(2\pi/L_x)^{1/3}$, as observed in figure 23. In the above expressions, the convergence of the Fourier transform requires that $\beta < 0$.

For convenience, we define a function $C(n_1, n_2)$ that approximates the exponent of the convolution of two functions f_1 and f_2 with the piecewise power-law spectra defined above in (5.5) and large-scale exponents $\alpha = n_1$ and $\alpha = n_2$, respectively, i.e. $\widehat{f_1 f_2} \sim m^{C(n_1,n_2)}$ for $m < m_0$. Here, we assume that $C(n_1, n_2)$ is independent of the small-scale exponents, as confirmed numerically in figure 25, and determine this quantity from a power-law fit to the convolution in the range $k \lesssim m \lesssim m_0$. Thus $C(n_1, n_2)$ is determined empirically.

Assuming that the fluctuation and mean fields are well approximated for $k \lesssim m \lesssim m_0$ by the power laws

$$\hat{\psi}' \sim m^a, \quad \hat{\bar{\psi}} \sim m^b, \quad \hat{S}' \sim m^c \quad \text{and} \quad \hat{\bar{S}} \sim m^d, \tag{5.6a–d}$$

and that $k \ll 1$ is fixed, a balance of the exponents in (5.3)–(5.4) implies

$$c = a - 2, \tag{5.7a}$$
$$C(b+1, a+2) = a - 1, \tag{5.7b}$$
$$C(a+1, a) = b + 2, \tag{5.7c}$$
$$C(a, c) = d + 1. \tag{5.7d}$$

These balances are obtained from fits to the data for wavenumbers m smaller than the breakpoint m_0, but not too small (since $m \gtrsim k$), and are therefore empirical. We solve (5.7) using an iterative process employing the fitting procedure described above to compute $C(a, b)$ for each a, b. The choice

$$a \approx 2, \quad b \approx -3, \quad c \approx 0, \quad d \approx -1 \tag{5.8a–d}$$

is found to lead to smallest error in (5.7) and matches well the numerical results for the mean velocity and salinity spectra presented in figure 20(*a*,*b*). Thus despite its

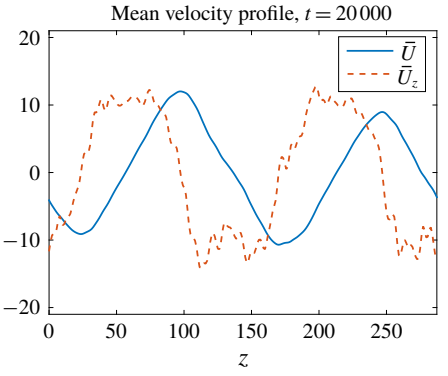

FIGURE 26. (Colour online) Mean velocity $\bar{U}$ and shear $\bar{U}_z$ for the full MRBC system at $t = 20\,000$.

empirical nature the above procedure provides a pathway to understanding the origin of the observed large-scale behaviour of the jet spectrum.

In figure 25 we show the matching between the numerical simulation results and the theoretical prediction for the left-hand side of (5.3*b*) and hence (5.7*b*). The convolution of functions of the form of (5.5) is well approximated by a power law in the large-scale regime. In addition, since the $\beta = -10$ and $\beta = -\infty$ cases are indistinguishable at large scales, we conclude that the small-scale exponent is unimportant in the computation of C. This provides a plausible explanation why the three systems – MRBC, quasilinear and single mode – all have the same large-scale spectrum, even though their small-scale spectra are very different.

We close this section by discussing the physical space structure corresponding to the large-scale scaling (5.8), focusing on the mean velocity $\bar{U}$ characterizing the jet structure. In view of the scaling $\hat{\bar{\psi}} \sim m^{-3}$ of the mean streamfunction, the mean velocity scales as $\hat{\bar{U}} \sim m^{-2}$. The inverse-square dependence of the spectrum of the jet velocity $\bar{U}$ on the wavenumber m is consistent with a zigzag profile: at the jet flank the mean velocity depends linearly on z and the shear is therefore constant, $\bar{U}_z = \text{const.}$, a conclusion that is confirmed in figure 26. Similar linkage between a power-law spectrum and spatial structure also appears in other systems. For example, the Phillips spectrum is based on the assumption that gravity waves have a wedge shape (Phillips 1958).

6. Turbulent Hopf bifurcation

One striking phenomenon observed in the simulations of the MRBC system (2.1), beyond the appearance of jets, is the turbulent state with superposed, approximately periodic oscillations present when $Ra = 6$. In contrast, when $Ra = 2$ these oscillations are absent and the state is statistically steady, albeit turbulent. An intriguing question arises therefore as to the mechanism whereby these oscillations first appear as Ra increases from $Ra = 2$. This section is devoted to this question.

Figure 27 shows the projection of the MRBC dynamics on two quantities characteristic of the large-scale dynamics, the kinetic energy K_{jet} in the jets and the salinity potential energy P_S, for four values of the Rayleigh ratio, $Ra = 2$, 3, 4 and 6. We see that when $Ra = 2$ the system evolves towards a fixed-point attractor

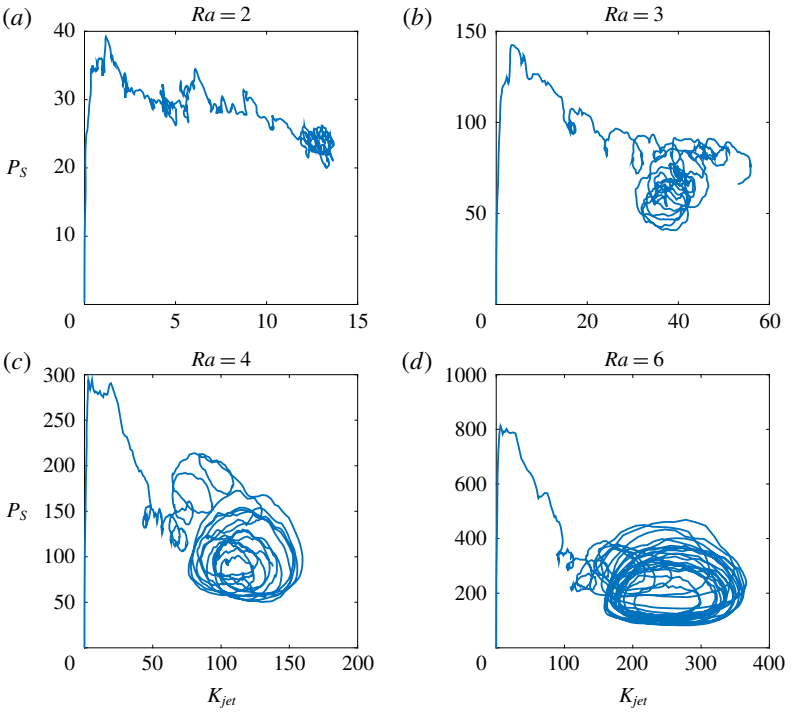

FIGURE 27. (Colour online) Projection of the MRBC dynamics on the salinity potential energy P_S and the kinetic energy K_{jet} in the jets within the time range $t \in [0,\ 2000]$ as computed from the MRBC system (2.1) with $Sc = 1$ and (*a–d*) $Ra = 2,\ 3,\ 4,\ 6$, respectively. All curves start close to $(0, 0)$.

corresponding to a statistically steady state. As Ra increases, an attractor remains but becomes a statistical limit cycle, corresponding to the appearance of oscillations with a well-defined period, cf. figure 2.

6.1. *Phenomenological model*

The basic mechanism for the saturation of the MRBC model is as follows: if nonlinear advection is absent, the linear dynamics indicate that the energy of the growing (respectively damped) modes increases (respectively decreases) exponentially; nonlinear advection couples these modes by transferring energy from the linearly growing modes to the linearly damped modes via the horizontally averaged mode, the jet mode. Based on the above considerations, we propose a three-component phenomenological model consisting of one linearly growing mode (A), one linearly damped mode (B) and one mean mode (C):

$$A_t = \lambda A - eCA - \alpha CB, \tag{6.1a}$$

$$B_t = -\delta B - eCB + \alpha CA, \tag{6.1b}$$

$$C_t = -dC + A^2 + B^2, \tag{6.1c}$$

where λ is the growth rate, δ is the damping rate, d is the decay rate of the mean mode and α and e capture the strength of stable–unstable and mean–fluctuation

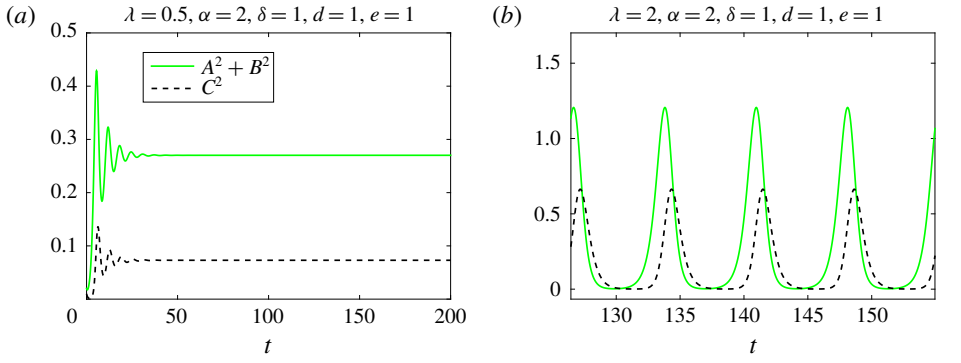

FIGURE 28. (Colour online) Energy evolution in the three-mode model (6.1) with the parameters $\alpha = 2$, $\delta = 1$, $d = 1$, $e = 1$ and (*a*) $\lambda = 0.5$, (*b*) $\lambda = 1$. In (*b*) we only show a window of the final periodic state.

interactions, respectively. The form of the nonlinear terms preserves total energy $E = (A^2 + B^2 + eC^2)/2$ when the linear terms are absent. The signs in front of $A^2 + B^2$ in the third equation and αCA in the second equation have been taken to be the same, so that in steady state perturbation energy is transferred from the linearly growing mode A to the linearly damped mode B; moreover, this sign must be opposite to that in front of the e-terms, while the signs of the two α-terms are opposite, ensuring that the nonlinear terms preserve energy. Although we can set two coefficients in the above model to be unity, e.g. $d = e = 1$, by an appropriate rescaling of the variables and the time scale, we do not do so here as some of the coefficients have clear physical meanings that we hope to explore in future work. We remark that this model has been developed to describe the strongly driven turbulent regime and so differs from other models of convectively driven shear flows that are based on the interaction between near-marginal modes (Howard & Krishnamurti 1986; Hughes & Proctor 1990; Rucklidge & Matthews 1996).

In this model, we expect the linear growth rate λ to be an increasing function of Ra and therefore show in figure 28 numerical solutions of (6.1) for different λ but keeping the other parameters fixed: $\alpha = 2$, $\delta = 1$, $d = 1$ and $e = 1$. This simple case study shows that when the growth rate is small, $\lambda = 0.5$, corresponding to small Ra, a steady state is reached, while for slightly larger growth rate, $\lambda = 1$, corresponding to a larger Ra, a periodic state is reached. In this state a phase lag between the wave and the mean, resembling that in the bottom panel in figure 2, is also observed.

Although the model (6.1) is based on our understanding of the energy transfer and is not asymptotically derived, its simple form enables us to carry out a detailed analysis. The steady state of the model is given by

$$A_0^2 = \frac{d\lambda}{(1+\beta^2)(e+\alpha\beta)}, \tag{6.2a}$$

$$B_0^2 = \frac{d\lambda\beta^2}{(1+\beta^2)(e+\alpha\beta)}, \tag{6.2b}$$

$$C_0 = \frac{\lambda}{(e+\alpha\beta)}, \tag{6.2c}$$

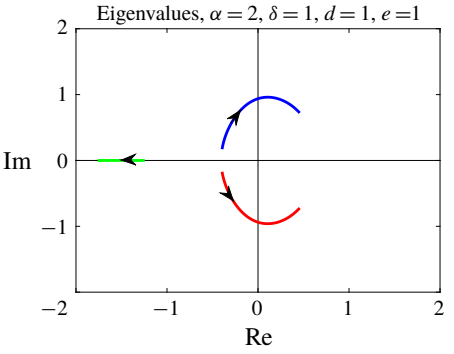

FIGURE 29. (Colour online) The eigenvalues of the nonlinear steady state of the model (6.1) with $\alpha = 2$, $\delta = 1$, $d = 1$, $e = 1$ and λ in the range [0.2, 2]. The arrows indicate the direction of increasing λ.

where

$$\beta = \frac{1}{2\delta\alpha}\left[-e(\delta+\lambda) + \sqrt{e^2(\delta+\lambda)^2 + 4\lambda\delta\alpha^2}\right]. \tag{6.3}$$

This state is stable for small λ, as shown in figure 28(*a*), but not for larger λ. To demonstrate this we examine the linear stability of this state described by the matrix

$$\boldsymbol{L} = \begin{pmatrix} \lambda - eC_0 & -\alpha C_0 & -eA_0 - \alpha B_0 \\ \alpha C_0 & -1 - eC_0 & \alpha A_0 - eB_0 \\ 2A_0 & 2B_0 & -d \end{pmatrix}. \tag{6.4}$$

Figure 29 shows the parameter dependence of the eigenvalues of $\boldsymbol{L}$ on λ with the other parameters held fixed. As λ increases, two eigenvalues cross the imaginary axis from left to right, indicating a (supercritical) Hopf bifurcation that we identify with the appearance of the statistical limit cycle observed in the numerical simulations of the MRBC model in figure 27. We mention that other examples of oscillatory instability of a turbulent state are known (e.g. Mujica & Lathrop 2015; Fauve *et al.* 2017).

7. Summary and discussion

In this paper we have studied the MRBC system (2.1) that describes salt-finger convection in the regime of strong forcing by the unstable salinity stratification and low salinity diffusivity. The system resembles Rayleigh–Bénard convection but includes dissipation on large scales arising from thermal effects. As a result instability sets in with an intrinsic length scale that is unrelated to externally imposed scales.

We have shown that the MRBC system, asymptotically valid in the limit $\tau \to 0$, evolves towards a structure consisting of horizontal jets which disrupt the salt-finger field and coarsen with increasing time. In the final, statistically steady state the large-scale jet structures coexist dynamically with small-scale fluctuations. Although our calculations were carried out for Schmidt number $Sc = 1$, we believe that this value captures the essential dynamics of the system, since it lies between the case $Sc \to \infty$ studied by Xie *et al.* (2017) and the opposite extreme case $Sc \to 0$ in which the temperature field is no longer slaved to the dynamics and therefore cannot be eliminated. The latter regime is neither geophysically nor astrophysically relevant,

however, although it could apply to isothermal systems with competing salt–sugar stratification.

We confirmed the validity of the MRBC system as a model of salt-finger convection by comparing the results of numerical simulations of the model with those of the primitive equations for Rayleigh ratio $Ra = 6$ carried out by Garaud & Brummell (2015) and corresponding to salinity forcing of intermediate strength. The comparison between these two simulations reveals common features, and in particular the presence of relaxation oscillations: the fingers force the jets, while the jets shear the fingers, and these two processes occur out of phase. However, we are unable to provide a quantitative explanation of the oscillation period observed by Garaud & Brummell (2015) because in our scaling we take κ_T to infinity while the primitive simulations employ a time scale based on the thermal time.

The case $Ra = 2$, corresponding to a larger density ratio, is expensive for direct numerical simulation of the primitive equations but is easily accessible in the MRBC system. In our simulations, initialized with small-amplitude random noise, we observe that the jet dynamics consist of two stages: the first stage is dominated by the linear salt-finger instability and the jets are weak. In this stage the energy concentrates around the optimal linear wavenumber and the nonlinear term transfers energy gradually away from the linearly unstable wavenumbers. In the second and later stage, the jets are strong and the kinetic energy concentrates around the marginal modes. A statistically steady state is reached through energy transport from the linearly growing wavenumbers to linearly damped wavenumbers via the mean field. Simultaneously, the jets coarsen to smaller wavenumbers, leading to more and more kinetic energy in the jet mode. Our simulations indicate that during the coarsening process the kinetic energy grows with the decreasing wavenumber of the jet structure as $K_{tot} \sim m_{dominant}^{-5/3}$ as the system extracts potential energy from the unstable salinity field.

To understand the mechanism of jet formation, we studied two further reductions of the MRBC system: a quasilinear system in which fluctuation–fluctuation interactions are omitted, and a single-mode system which retains only one horizontal wavenumber in the fluctuations, the wavenumber corresponding to the domain-filling mode. The major finding is that even these highly simplified systems both generate jets, thereby confirming that the formation and maintenance of jets by the fluctuating fields is a consequence of mean–fluctuation interactions. However, the two systems do differ in some details from the MRBC system: the jets in the quasilinear system exhibit greater temporal variability and coarsen more slowly as compared with those in the MRBC system. In the single-mode model, temporal variability also includes intermittent bursts in the energy evolution.

Even though the details of the three systems are different, the energy spectra of the jets show a uniform wavenumber scaling at large scales, $E_u \sim m^{-4}$ and $E_S \sim m^{-2}$, which enables us to use the one-dimensional balances in the single-mode system to study the formation and properties of the jet state. For the fluctuations, the dominant balance in the momentum equation is between energy pumping through the buoyancy term and large-scale damping; at next order advective transport accounts for the remaining imbalance. In the salinity equation, the flux, damping and transport terms all contribute to the leading-order balance. In contrast, in the mean-field equations, both the momentum and salinity equations have the same basic balance between nonlinear advection by the fluctuations and damping. A piecewise power-law model for the spectrum (5.5) was shown to capture self-consistently the observed spectra of both the mean and the fluctuating fields at large vertical scales. In particular, the

observed scaling $E_u \sim m^{-4}$ indicates that the jets have a zigzag velocity profile, a prediction also consistent with the DNS studies. Based on the above balances we used phenomenological arguments to propose a simple three-variable model that appears to capture the basic properties of the statistically stationary state and its loss of stability to oscillations with increasing Rayleigh ratio.

The jet formation and subsequent coarsening process observed in the MRBC system are reminiscent of other two-dimensional systems with both small-scale and large-scale dissipation. The prototypical system of this type is provided by the two-dimensional vorticity equation with small-scale dissipation and large-scale damping analogous to Rayleigh friction and driven by an externally imposed small-scale random force (Smith & Yakhot 1994; Bouchet & Simonnet 2009; Laurie *et al.* 2014; Frishman 2017; Frishman *et al.* 2017). This system exhibits spectral condensation into domain-size vortex structures in square domains and into parallel jets in rectangular domains. In both cases these structures are long-time statistically stationary states of the system that are both maintained by and in equilibrium with the small-scale fluctuations introduced by the random force. In fact, similar phenomenology is also observed in three-dimensional but highly anisotropic systems, such as thin-layer turbulence (Francois *et al.* 2013; Xia & Francois 2017) and rapidly rotating Rayleigh–Bénard convection (Guervilly & Hughes 2017; Julien, Knobloch & Plumley 2018). Because of the strongly anisotropic motions, both these systems behave like two-dimensional systems. However, in both, the domain-size structures are in equilibrium with the small-scale fluctuations they themselves generate, as opposed to externally imposed fluctuations, exactly as in the MRBC system studied here. In each case the jets are statistical structures and so are contaminated by transient vortices and other small-scale features, as also observed in the MRBC system.

One may expect that some understanding of the spectral condensation process may be achieved using equilibrium statistical mechanics (Bouchet & Simonnet 2009; Bouchet & Venaille 2012), as in other systems of this type (Julien *et al.* 2018), despite the fact that these systems are driven dissipative systems and so are not equilibrium systems in the statistical mechanics sense. However, the MRBC system is in fact far from equilibrium because the salinity field is not a passive scalar and is coupled to the streamfunction bidirectionally. As a result the buoyancy force does not behave like an external random force. Despite these essential differences, similarities between these systems remain and these can be traced to the presence of strong anisotropy: in contrast to the vorticity equation with large-scale but isotropic damping, the MRBC system has anisotropic large-scale dissipation that mimics the anisotropy introduced in the stochastically forced two-dimensional vorticity equation via the domain aspect ratio (Bouchet & Simonnet 2009; Bouchet & Venaille 2012; Falkovich 2016; Frishman *et al.* 2017).

We close this paper with remarks on four future directions. First, the details of the coarsening process of the jets observed in the MRBC system, such as the mechanism behind coarsening, its time scale and the final jet scale, still remain to be understood. Second, assuming an equilibrium jet scale exists, its dependence on the external parameters needs to be determined. In fact, from the balance between the nonlinear and the large-scale damping terms in the mean-momentum equation we obtain a characteristic length scale,

$$\ell = \left(\frac{U_{rms}}{Sc}\right)^{1/3} \left(\text{dimensional: } l^* = \left(\frac{U^*_{rms}\kappa_T\kappa_S^2}{g\alpha_T\beta_T}\right)^{1/3}\right), \tag{7.1}$$

that may play a similar role to the Rhines scale for β-plane jets (Rhines 1975). Evidently, studies of the MRBC system for different values of the Schmidt number are desirable. Third, the validation of the phenomenological model (6.1) requires that its parameters be fixed by numerical data or theory in order to facilitate further study of bifurcations of the turbulent jet state. Fourth, the present work has focused on the two-dimensional dynamical MRBC model, and it is an open question whether the results we find in this paper generalize to three dimensions. A three-dimensional MRBC model is easily derived following Xie *et al.* (2017), but isotropy in the horizontal plane may prevent the formation of coherent horizontal jets (Garaud & Brummell 2015). However, a preferred direction may be selected through the use of a rectangular domain in the horizontal, as done for example by Guervilly & Hughes (2017) and Julien *et al.* (2018), and in this case coherent jets may still form.

Acknowledgements

We are grateful to three anonymous referees for suggestions that improved the presentation of this work. The work was supported in part by the National Science Foundation through grants DMS-1317596 (J.-H.X. and E.K.) and DMS-1317666 (K.J.). J.-H.X. also acknowledges financial support from the Office of Naval Research through grant N00014-15-1-2355.

REFERENCES

BALMFORTH, N. J., LLEWELLYN SMITH, S. G. & YOUNG, W. R. 1998 Dynamics of interfaces and layers in a stratified turbulent fluid. *J. Fluid Mech.* **355**, 329–358.

BEAUME, C., CHINI, G. P., JULIEN, K. & KNOBLOCH, E. 2015 Reduced description of exact coherent states in parallel shear flows. *Phys. Rev.* E **91**, 043010.

BOUCHET, F. & SIMONNET, E. 2009 Random changes of flow topology in two-dimensional and geophysical turbulence. *Phys. Rev. Lett.* **102**, 094504.

BOUCHET, F. & VENAILLE, A. 2012 Statistical mechanics of two-dimensional and geophysical flows. *Phys. Rep.* **515**, 227–295.

BROWN, J. M., GARAUD, P. & STELLMACH, S. 2013 Chemical transport and spontaneous layer formation in fingering convection in astrophysics. *Astrophys. J.* **768**, 34.

BRUMMELL, N. H. & HART, J. E. 1993 High Rayleigh number β-convection. *Geophys. Astrophys. Fluid Dyn.* **68**, 85–114.

BUSSE, F. H. 1983 A model of mean zonal flows in the major planets. *Geophys. Astrophys. Fluid Dyn.* **23**, 153–174.

CHILDRESS, S. 2000 Eulerian mean flow from an instability of convective plumes. *Chaos* **10**, 28–38.

CHONG, K. L., YANG, Y., HUANG, S.-D., ZHONG, J.-Q., STEVENS, R. J. A. M., VERZICCO, R., LOHSE, D. & XIA, K.-Q. 2017 Confined Rayleigh–Bénard, rotating Rayleigh–Bénard, and double diffusive convection: a unifying view on turbulent transport enhancement through coherent structure manipulation. *Phys. Rev. Lett.* **119**, 064501.

DENISSENKOV, P. A. 2010 Numerical simulations of thermohaline convection: implications for extra-mixing in low-mass RGB stars. *Astrophys. J.* **723**, 563–579.

FALKOVICH, G. 2016 Interaction between mean flow and turbulence in two dimensions. *Proc. R. Soc. Lond.* A **472**, 20160287.

FARRELL, B. F. & IOANNOU, P. J. 2003 Structural stability of turbulent jets. *J. Atmos. Sci.* **50**, 2101–2118.

FARRELL, B. F. & IOANNOU, P. J. 2007 Structure and spacing of jets in barotropic turbulence. *J. Atmos. Sci.* **64**, 3652–3665.

FAUVE, S., HERAULT, J., MICHEL, G. & PÉTRÉLIS, F. 2017 Instabilities on a turbulent background. *J. Stat. Mech.: Theory Exp.* **6**, 064001.

FERNANDES, A. M. & KRISHNAMURTI, R. 2010 Salt finger fluxes in a laminar shear flow. *J. Fluid Mech.* **658**, 148–165.

FITZGERALD, J. G. & FARRELL, B. F. 2014 Mechanisms of mean flow formation and suppression in two-dimensional Rayleigh–Bénard convection. *Phys. Fluids* **26**, 054104.

FRANCOIS, N., XIA, H., PUNZMANN, H. & SHATS, M. 2013 Inverse energy cascade and emergence of large coherent vortices in turbulence driven by Faraday waves. *Phys. Rev. Lett.* **110**, 194501.

FRISHMAN, A. 2017 The culmination of an inverse cascade: mean flow and fluctuations. *Phys. Fluids* **29**, 125102.

FRISHMAN, A., LAURIE, J. & FALKOVICH, G. 2017 Jets or vortices: What flows are generated by an inverse turbulent cascade? *Phys. Rev. Fluids* **2**, 032602(R).

GARAUD, P. 2018 Double-diffusive convection at low Prandtl number. *Annu. Rev. Fluid Mech.* **50**, 275–298.

GARAUD, P. & BRUMMELL, N. 2015 2D or not 2D: the effect of dimensionality on the dynamics of fingering convection at low Prandtl number. *Astrophys. J.* **815**, 42.

GOLUSKIN, D., JOHNSTON, H., FLIERL, G. R. & SPIEGEL, E. A. 2014 Convectively driven shear and decreased heat flux. *J. Fluid Mech.* **795**, 360–385.

GUERVILLY, C. & HUGHES, D. W. 2017 Jets and large-scale vortices in rotating Rayleigh–Bénard convection. *Phys. Rev. Fluids* **2**, 113503.

VON HARDENBERG, J., GOLUSKIN, D., PROVENZALE, A. & SPIEGEL, E. A. 2015 Generation of large-scale winds in horizontally anisotropic convection. *Phys. Rev. Lett.* **115**, 134501.

HERMIZ, K. B., GUZDAR, P. N. & FINN, J. M. 1995 Improved low-order model for shear flow driven by Rayleigh–Bénard convection. *Phys. Rev.* E **51**, 325–331.

HOLYER, J. Y. 1984 The stability of long, steady, two-dimensional salt fingers. *J. Fluid Mech.* **147**, 169–185.

HORTON, W., HU, G. & LAVAL, G. 1996 Turbulent transport in mixed states of convective cells and sheared flows. *Phys. Plasmas* **3**, 2912–2923.

HOWARD, L. N. & KRISHNAMURTI, R. 1986 Large-scale flow in turbulent convection: a mathematical model. *J. Fluid Mech.* **170**, 385–410.

HUGHES, D. W. & PROCTOR, M. R. E. 1990 A low-order model of the shear instability of convection: chaos and the effect of noise. *Nonlinearity* **3**, 127–153.

JULIEN, K., KNOBLOCH, E. & PLUMLEY, M. 2018 Impact of domain anisotropy on the inverse cascade in geostrophic turbulent convection. *J. Fluid Mech.* **834**, R4.

KRISHNAMURTI, R. & HOWARD, L. N. 1981 Large-scale flow generation in turbulent convection. *Proc. Natl Acad. Sci. USA* **78**, 1981–1985.

LAURIE, J., BOFFETTA, G., FALKOVICH, G., KOLOKOLOV, I. & LEBEDEV, V. 2014 Universal profile of the vortex condensate in two-dimensional turbulence. *Phys. Rev. Lett.* **113**, 254530.

LINDEN, P. F. 1974 Salt fingers in a steady shear flow. *Geophys. Fluid Dyn.* **6**, 1–27.

MALKUS, W. V. R. 1954 The heat transport and spectrum of thermal turbulence. *Proc. R. Soc. Lond.* A **225**, 185–195.

MARSTON, J. B., CONOVER, E. & SCHNEIDER, T. 2008 Statistics of an unstable barotropic jet from a cumulant expansion. *J. Atmos. Sci.* **65**, 1955–1966.

MATTHEWS, P. C., PROCTOR, M. R. E., RUCKLIDGE, A. M. & WEISS, N. O. 1993 Pulsating waves in nonlinear magnetoconvection. *Phys. Lett.* A **183**, 69–75.

MATTHEWS, P. C., RUCKLIDGE, A. M., WEISS, N. O. & PROCTOR, M. R. E. 1996 The three-dimensional development of the shearing instability. *Phys. Fluids* **8**, 1350–1352.

MERRYFIELD, W., HOLLOWAY, G. & GARGETT, A. 1999 A global ocean model with double-diffusive mixing. *J. Phys. Oceanogr.* **29**, 1124–1142.

MUJICA, N. & LATHROP, D. P. 2015 Hysteretic gravity-wave bifurcation in a highly turbulent swirling flow. *J. Fluid Mech.* **551**, 49–62.

O'GORMAN, P. A. & SCHNEIDER, T. 2007 Recovery of atmospheric flow statistics in a general circulation model without nonlinear eddy–eddy interactions. *Geophys. Res. Lett.* **34**, L22801.

PAPARELLA, F. & VON HARDENBERG, J. 2012 Clustering of salt fingers in double-diffusive convection leads to staircaselike stratification. *Phys. Rev. Lett.* **109**, 014502.

PAPARELLA, F. & SPIEGEL, E. A. 1999 Sheared salt fingers: instability in a truncated system. *Phys. Fluids* **11**, 1161–1168.

PHILLIPS, O. M. 1958 The equilibrium range in the spectrum of wind-generated waves. *J. Fluid Mech.* **4**, 426–434.

PRAT, V., LIGNIÈRES, F. & LAGARDE, N. 2015 Numerical simulations of zero-Prandtl-number thermohaline convection. In *SF2A-2015: Proceedings of the Annual meeting of the French Society of Astronomy and Astrophysics*, pp. 419–422. Société Française d'Astronomie et d'Astrophysique.

RADKO, T. 2003 A mechanism for layer formation in a double-diffusive fluid. *J. Fluid Mech.* **497**, 365–380.

RADKO, T. 2008 The double-diffusive modon. *J. Fluid Mech.* **609**, 59–85.

RADKO, T. 2010 Equilibration of weakly nonlinear salt fingers. *J. Fluid Mech.* **645**, 121–143.

RADKO, T. 2013 *Double-diffusive Convection*. Cambridge University Press.

RADKO, T., BALL, J., COLOSI, J. & FLANAGAN, J. 2015 Double-diffusive convection in a stochastic shear. *J. Phys. Oceanogr.* **45**, 3155–3167.

RADKO, T. & SMITH, D. P. 2012 Equilibrium transport in double-diffusive convection. *J. Fluid Mech.* **692**, 5–27.

RADKO, T. & STERN, M. E. 1999 Salt fingers in three dimensions. *J. Mar. Res.* **57**, 471–502.

RHINES, P. B. 1975 Waves and turbulence on a beta-plane. *J. Fluid Mech.* **69**, 417–443.

RUCKLIDGE, A. M. & MATTHEWS, P. C. 1996 Analysis of the shearing instability in nonlinear convection and magnetoconvection. *Nonlinearity* **9**, 311–351.

SCHMITT, R. W. 1983 The characteristics of salt fingers in a variety of fluid systems, including stellar interiors, liquid metals, oceans, and magmas. *Phys. Fluids* **26**, 2373–2377.

SCHMITT, R. W. 1994 Double diffusion in oceanography. *Annu. Rev. Fluid Mech.* **26**, 255–285.

SHEN, C. Y. 1995 Equilibrium salt-fingering convection. *Phys. Fluids* **7**, 704–717.

SMITH, L. M. & YAKHOT, V. 1994 Finite-size effects in forced two-dimensional turbulence. *J. Fluid Mech.* **274**, 115–138.

SMYTH, W. & KIMURA, S. 2007 Instability and diapycnal momentum transport in a double-diffusive, stratified shear layer. *J. Phys. Oceanogr.* **37**, 1551–1565.

SRINIVASAN, K. & YOUNG, W. R. 2012 Zonostrophic instability. *J. Atmos. Sci.* **69**, 1633–1656.

STELLMACH, S., TRAXLER, A., GARAUD, P., BRUMMELL, N. & RADKO, T. 2011 Dynamics of fingering convection. Part 2. The formation of thermohaline staircases. *J. Fluid Mech.* **677**, 554–571.

STERN, M. E. 1960 The salt-fountain and thermohaline convection. *Tellus* **12**, 172–175.

STERN, M. E. 1969 Collective instability of salt fingers. *J. Fluid Mech.* **35**, 209–218.

STERN, M. E. & RADKO, T. 1998 The salt finger amplitude in unbounded T–S gradient layers. *J. Mar. Res.* **56**, 157–196.

TRAXLER, A., GARAUD, P. & STELLMACH, S. 2011*a* Numerically determined transport laws for fingering ('thermohaline') convection in astrophysics. *Astrophys. J.* **728**, L29.

TRAXLER, A., STELLMACH, S., GARAUD, P., RADKO, T. & BRUMMELL, N. 2011*b* Dynamics of fingering convection. Part 1. Small-scale fluxes and large-scale instabilities. *J. Fluid Mech.* **677**, 530–553.

TURNER, J. S. 1974 Double diffusive phenomena. *Annu. Rev. Fluid Mech.* **6**, 37–54.

XIA, H. & FRANCOIS, N. 2017 Two-dimensional turbulence in three-dimensional flows. *Phys. Fluids* **29**, 111107.

XIE, J.-H., KNOBLOCH, E., MIQUEL, B. & JULIEN, K. 2017 A reduced model for salt-finger convection in the small diffusivity ratio limit. *Fluids* **2** (1), 6.